

Metallicity of Active Galactic Nuclei from ultraviolet and optical emission lines – II. Revisiting the C43 metallicity calibration and its implications

O. L. Dors¹ , C. B. Oliveira¹, M. V. Cardaci^{2,3}, G. F. Hägele^{2,3}, Mark Armah¹, R. A. Riffel⁴, L. Ramos Vieira^{4,5}, G. C. Almeida¹, I. N. Morais¹, P. C. Santos¹

¹Universidade do Vale do Paraíba, Av. Shishima Hifumi, 2911, Cep 12244-000, São José dos Campos, SP, Brazil

²Facultad de Ciencias Astronómicas y Geofísicas, Universidad Nacional de La Plata, Paseo del Bosque s/n, 1900 La Plata, Argentina.

³Instituto de Astrofísica de La Plata (CONICET-UNLP), La Plata, Avenida Centenario (Paseo del Bosque) S/N, B1900FWA, Argentina

⁴Departamento de Física, Centro de Ciências Naturais e Exatas, Universidade Federal de Santa Maria, 97105-900, Santa Maria, RS, Brazil

⁵Instituto Federal Catarinense - Campus Concórdia, 89703-720, Concórdia, SC, Brazil

Accepted XXX. Received YYY; in original form ZZZ

ABSTRACT

In this study, a new semi-empirical calibration is proposed between ultraviolet emission lines ($\text{C III}\lambda 1909$, $\text{C IV}\lambda 1549$, $\text{He II}\lambda 1640$) of type 2 AGNs and their metallicity (Z). This calibration is derived by comparing a large sample of 106 objects (data taken from the literature) located over a wide range of redshifts ($0 \lesssim z \lesssim 4.0$) with predictions from photoionization models that adopt a recent C/O–O/H relation derived via estimates using the T_e method, which is considered the most reliable method. We found that the new calibration produces Z values in agreement (within an uncertainty of ± 0.1 dex) with those from other calibrations and from estimates via the T_e -method. We find also that AGN metallicities are already high at early epochs, with no evidence for monotonic evolution across the redshift range $0 \lesssim z \lesssim 12$. Notably, the highest metallicities in our sample, reaching up to $4 Z_\odot$, are found in objects at $2 \lesssim z \lesssim 3$. This redshift range coincides with the peak of the cosmic star formation rate history, suggesting a strong connection between the major epoch of star formation, black hole growth, and rapid metal enrichment in the host galaxies of AGNs. Furthermore, our analysis reveals no significant correlation between AGN metallicity and radio properties (radio spectral index or radio luminosity) or host galaxy stellar mass. The lack of a clear mass-metallicity relation, consistent with findings for local AGNs, suggests that the chemical evolution of the nuclear gas is decoupled from the global properties of the host galaxy.

Key words: galaxies: Seyfert – galaxies: active – galaxies: abundances –ISM: abundances –galaxies: evolution –galaxies: nuclei

1 INTRODUCTION

Metallicity (Z) estimations based on emission lines are essential for understanding the chemical evolution of galaxies, stellar nucleosynthesis and the interplay between stars and the interstellar medium (ISM) over the Hubble time. Observations from ground-based telescopes, combined with recent data from the James Webb Space Telescope (JWST), have enabled the estimation of Z in the gas-phase of objects across a wide range of redshifts (e.g. $0 \leq z \lesssim 14$; Carniani et al. 2024), revolutionizing our understanding of the chemical enrichment of the Universe.

The methods for estimating Z depend on the set of emission lines available and on their wavelength range (for a review, see Maiolino & Mannucci 2019; Kewley et al. 2019). For objects at $z \lesssim 0.4$, where most observational data are in the optical range $[3000 \text{ } \text{\AA} < \lambda(\text{\AA}) < 7000$; e.g. York et al. 2000; Sánchez et al. 2012; Bundy et al. 2015; Berg et al. 2015], the most reliable method is the T_e -method or the direct method, known to have been developed by Peimbert & Costero (1969). Summar-

ily, this method is based on the estimation of the electron temperature through auroral lines (e.g. $[\text{O III}]\lambda 4363$), which are about 100 times weaker than $\text{H}\beta$ and measured mainly in spectra of objects with low metallicity ($Z \lesssim Z_\odot$) and/or with high excitation (e.g. van Zee et al. 1998; Kennicutt et al. 2003; Hägele et al. 2008; Rogers et al. 2022; Gavilán et al. 2025). To circumvent the difficulty of applying the T_e -method, Pagel et al. (1979), following the original idea of Jensen et al. (1976), proposed the strong-line method — a calibration between the $R_{23} = [\text{O II}]\lambda 3727 + [\text{O II}]\lambda 4959 + \lambda 5007]/\text{H}\beta$ line ratio and the oxygen abundance in relation to hydrogen (O/H, a Z tracer). Both the T_e -method and the strong-line methods have been adapted for active galactic nuclei (AGNs) by Dors et al. (2020b) and Storchi-Bergmann et al. (1998), respectively. In particular, AGNs are bright objects that can be used to trace the Z evolution of the Universe instead of star-forming galaxies, hence a large number of active galaxies has been observed in the local universe (e.g. Koski 1978; Dopita et al. 2015; Kakkad et al. 2018; Revalski et al. 2018; Brown et al. 2019; Senarath et al. 2021; Durré & Mould 2022; Menezes et al. 2022) and at $z \gtrsim 5$ (e.g. Juodžbalis et al. 2023; Scholtz et al. 2023; Maiolino et al. 2024; Duan et al. 2024; Napolitano et al. 2025; D’Silva et al. 2025; Geris et al. 2025).

* E-mail: olidors@univap.br

Calibrations between emission line intensity ratios and Z can be obtained, mainly, by three methods, each with its own limitations, as summarized below.

- Empirical calibrations: consist of a calibration between a given emission line ratio (e.g. R_{23}) and abundance estimates (e.g. O/H) derived from the T_e -method (e.g. Pilyugin 2000, 2001; Jiang et al. 2019; Dors 2021; Gavilán et al. 2025). The main advantage of this method is to use reliable abundance values (by using the T_e -method). However, these calibrations are restricted to using abundance estimates in objects that have spectra with a high signal-to-noise ratio, low Z , and detectable auroral lines (e.g. Hägele et al. 2006, 2008; Díaz et al. 2007).
- Theoretical calibrations: are based exclusively on photoionization models (e.g. McGaugh 1991; Kewley & Dopita 2002; Dors et al. 2014; Zhu et al. 2024), and the predicted emission line intensities (output) are calibrated with the metallicity considered in the models (input). The main advantage of this method is to cover a wide range of nebular parameters (e.g. Z , ionization parameter, electron density among others). However, uncertainties in the physical processes considered in photoionization models due to assumptions such as electron temperature distribution, spectral energy distribution, geometry, atomic parameters, etc., introduce several uncertainties in this kind of calibration (e.g. Dopita et al. 2013; Nicholls et al. 2017; Juan de Dios & Rodríguez 2017; Zhu et al. 2023; Li et al. 2024a,c; Binette et al. 2024; Koutsoumpou et al. 2025).
- Semi-empirical calibrations: are based on a comparison between results of photoionization models and observational emission line ratios of a sample of objects. From this comparison, it is possible to infer a relation between the Z values for the objects in the observational sample and their emission line intensity ratios (see Nagao et al. 2006b; Castro et al. 2017; Carvalho et al. 2020; Dors et al. 2013, 2019). The main advantage of this methodology is to minimize the effects of the unrealistic nebular parameters in the models, constraining them through the observational data. Moreover, these methods do not require direct abundance estimates, which increases the potential sample size. Such calibrations are affected by photoionization model uncertainties and to the sample size.

Another important factor is the spectral wavelength range necessary for the estimation of Z . For instance, in the optical range, several auroral emission lines (e.g. [O III]λ4363, [N II]λ5755) can be measured, allowing for direct Z estimates (i.e. to apply the T_e -method) and making it possible to obtain empirical relations (e.g. Pilyugin & Grebel 2016; Dors 2021). Otherwise, in the case of the ultraviolet (UV) range [$1000 < \lambda(\text{\AA}) < 3000$] direct abundance estimates are difficult or impossible to derive, requiring a combination with optical temperature estimates (e.g. Berg et al. 2016, 2024; Isobe et al. 2023; Rogers et al. 2023; Ji et al. 2024; Hsiao et al. 2024; Hu et al. 2024; Citro et al. 2024; Kumari et al. 2024b; Hayes et al. 2025). An additional challenge in abundance estimates using UV emission lines is the limited number of hydrogen line measurements, since the unique hydrogen line is Ly α , a highly resonance line (e.g. Shields et al. 1995; Humphrey 2019). This result in an imprecise dust reddening correction (generally not considered or taken from the Balmer decrement, e.g. Berg et al. 2016) and in elemental abundance estimates relative to helium (see Dors et al. 2022). In summary, reliable Z and metal abundance estimates from UV emission lines require both optical and UV spectroscopic data for the same source, which are available in the literature only for a few cases (e.g. Berg et al. 2016; Dors et al. 2025).

The above caveats show that Z estimates through only UV emission lines are subject to some uncertainties, as listed below. Photo-

ionization models are generally used to estimate Z from only UV emission lines, with the best emission line ratios used as Z indicators being under discussion in the field of nebular astrophysics (e.g. Nagao et al. 2006b; Zhu et al. 2024). Dors et al. (2014) suggested the $C43=(\text{C IV} \lambda 1549 + \text{C III} \lambda 1909)/\text{He II} \lambda 1640$ line ratio as Z indicator for Narrow Line Regions (NLRs) of AGNs. Theoretical calibrations relied on the $C43$ index, as well as other line ratios (e.g. Si III]λ1883, λ1892/C III]λ1909, N Vλ1240/He IIλ1640; see Hamann & Ferland 1992; Nagao et al. 2006b; Zhu et al. 2024), require the knowledge of abundance relations. For instance, calibrations involving carbon emission lines are highly dependent on the C/O–O/H relation assumed in the photoionization models. In particular, this relation was derived only for nearby H II regions (e.g. Garnett et al. 1999; Esteban et al. 2005, 2009, 2020; Dopita et al. 2006; Arellano-Córdova et al. 2020; Skillman et al. 2020), not necessarily valid for high- z objects (e.g. Ji et al. 2024) and/or AGNs (e.g. Pérez-Montero et al. 2023).

The scaling relations for the abundances of metals (e.g. C, N) as a function of total metallicity have been discussed in detail by Nicholls et al. (2017). These authors suggested using stellar abundance estimations to scale abundances with the total metallicity in nebular photoionization models. This approach has the advantage of producing abundance relations spanning over a wide range of oxygen abundances, i.e. $6.0 \lesssim 12 + \log(\text{O/H}) \lesssim 9.0$ [$0.002 \lesssim (Z/Z_\odot) \lesssim 2.0$] and, unlike most nebular abundances, stellar abundance relations are weakly affected by depletion of elements (e.g. C, O, Si) onto dust grains (e.g. Mathis 1986; Oliveira & Maciel 1986; Aannestad 1989; Shields & Kennicutt 1995; Garnett et al. 1995; Kingdon et al. 1995; Jenkins 2009; Gunasekera et al. 2022, 2023; Méndez-Delgado et al. 2024).

Recently, (Dors et al. 2025, hereafter Paper I), combined optical and UV data of AGNs (7 objects) together with a large sample of local H II regions (72 objects), and used the T_e -method to derive a C/O–O/H relation that showed deviations from those previously proposed in the literature adopting nebular (e.g. Dopita et al. 2006) and stellar (Nicholls et al. 2017) abundance estimates, in the sense that higher (~ 0.2 dex) C/O abundances are derived for the very high metallicity regime [$Z \gtrsim Z_\odot$ or $12 + \log(\text{O/H}) \gtrsim 8.7$]. The use of this new C/O–O/H relation to build photoionization models provides Z values from the $C43$ index for nearby AGNs in agreement with those via the T_e -method, highlighting the reliability of the derived abundance relation. In this subsequent study, we use the C/O–O/H relation derived in Paper I, combined with a large sample of type 2 AGN data, to provide a more reliable $C43$ – Z calibration for this class of active objects than previous ones (see e.g. Dors et al. 2014, 2019). This new calibration is applied to a large sample of AGNs in a wide redshift range ($0 \lesssim z \lesssim 12$), and the results are discussed in terms of the cosmic evolution of Z and its relation with the stellar mass of the host galaxy as well as radio spectral indexes. The paper is organized as follows. In Section 2 the methodology employed (observational data and photoionization models) to derive the new $C43$ – Z calibration is presented. The results and discussion are given in Sects. 3 and 4, respectively. The conclusion of the outcome is given in Sect. 5. Throughout this paper, we adopt the cosmological parameters by Planck Collaboration et al. (2021): $H_0 = 67.4 \text{ km s}^{-1} \text{ Mpc}^{-1}$ and $\Omega_m = 0.315$.

2 METHODOLOGY

To obtain a semi-empirical Z calibration, we use the C/O–O/H relation from Paper I as input for a grid of photoionization models

constructed with the CLOUDY code (Ferland et al. 2017). We then compare the model predictions with observational data on a $C\text{IV}$ versus $\text{C III}\lambda 1909/\text{C IV}\lambda 1549$ diagram (see also Arevalo Gonzalez et al. 2025). The procedure used to derive the calibration is described below.

2.1 Photoionization models

We constructed a grid of photoionization models simulating the NLRs of AGNs using version 23.01 of the CLOUDY code (Ferland et al. 2017). The input parameters for these models are described below.

- Spectral Energy Distribution (SED): is parametrized by the α_{ox} slope (Tananbaum et al. 1979), defined by

$$\alpha_{ox} = \frac{\log[F(2 \text{ kev})/F(2500 \text{ \AA})]}{\log[\nu(2 \text{ keV})/\nu(2500 \text{ \AA})]}, \quad (1)$$

where F is the flux at the given frequency ν . We assume $\alpha_{ox} = -1.1, -0.8$. The SED of an AGN depends mainly on the thermal emission from the surface of an accretion disk (e.g. Malkan & Sargent 1982; Cheng et al. 2019), on the thickness of the disk (e.g. Laor & Netzer 1989; Blaes 2014; Taylor & Reynolds 2018) and on the electron scattering (e.g. Czerny & Elvis 1987; Gutiérrez et al. 2021). Photoionization models assuming these α_{ox} values are able to reproduce UV (e.g. Dors et al. 2018), optical (e.g. Carvalho et al. 2020) and infrared (e.g. Calabro et al. 2023) emission line intensity ratios. In Carvalho et al. (2020), we found that models considering $\alpha_{ox} < -1.1$ result in emission line ratios lower than the observational ones; thus, these values were not considered.

A second ionization source by background cosmic rays with an ionization rate (default value in the CLOUDY code) of $2 \times 10^{-16} \text{ s}^{-1}$ (Indriolo et al. 2007) was adopted in the models. This source influences the heating of the interstellar medium and ionization of ions with low ionization potential (e.g. N^+ , see Koutsoumpou et al. 2025 and references therein). Also, a turbulence with velocity equal to 100 km s^{-1} (Ferland 1992) was adopted in the models. Basically, turbulence affects the shielding and pumping of lines in the sense that fluorescent excitation becomes more important for larger turbulent line widths.

- Metallicity (Z): the assumed values are $(Z/Z_\odot) = 0.1, 0.2, 0.5, 1.0, 2.0, 3.0$, and 4.0 . They cover the Z range derived for a large sample of AGNs with low (e.g. Groves et al. 2006; Pérez-Montero et al. 2019; do Nascimento et al. 2022; Li et al. 2024b; Armah et al. 2024), intermediate (e.g. Carr et al. 2023; Juodžbalis et al. 2024) and high (e.g. Pérez-Montero et al. 2023; Ji et al. 2024) redshifts, derived by using different methods (e.g. Dors et al. 2020a,b). As in the work by Nagao et al. (2006b), the models are dust free.

- Abundance relations: the abundances of all elements were linearly scaled with Z , with the exception of helium, nitrogen, and carbon, whose abundances were estimated from the relations derived through the T_e -method by Dors et al. (2022, 2024b, 2025) and given by:

$$\log(\text{N/O}) = 0.86 \times (x) - 8.39, \quad (x > 8.0), \quad (2)$$

$$\log(\text{N/O}) = -1.4, \quad (x < 8.0), \quad (3)$$

$$12 + \log(\text{He/H}) = 0.1215 \times (x^2) - 1.8183 \times (x) + 17.6732, \quad (4)$$

and

$$\log(\text{C/O}) = 0.41 \times (x^2) - 6.07 \times (x) + 21.69, \quad (5)$$

where $x = 12 + \log(\text{O/H})$.

- Electron density (N_e): three values of N_e were assumed: $100, 500$ and 3000 cm^{-3} , which represents the range of electron density values derived from the $[\text{S II}]\lambda 6716/\lambda 6731$ line ratio for NLRs (e.g. Rupke et al. 2017; Kakkad et al. 2018; Freitas et al. 2018; Mingozzi et al. 2019; Davies et al. 2020; Ilha et al. 2022; Zhang 2024).

- Ionization parameter (U): we consider the logarithm of the ionization parameter in the range of $-3.5 \leq \log U \leq -1.0$, with a step of 0.5 dex. Models assuming this range of values are able to reproduce observational data of AGNs with a wide range of ionization degree (e.g. Carvalho et al. 2020; Pérez-Montero et al. 2025). The geometry of the models is plane parallel and the outermost radius is that where the electron temperature reaches 4000 K (default value of the CLOUDY code).

In total, 216 photoionization models were built, covering a wide range of nebular parameters.

2.2 Observational data

Our sample consists of the same observational data compiled from the literature by Dors et al. (2014, 2019), supplemented with 30 Type 2 Quasars ($2.0 \leq z \leq 4.0$) from Silva et al. (2020), whose data were taken from the Sloan Digital Sky Survey III Baryon Oscillation Spectroscopic Survey (SDSS BOSS; Alexandroff et al. 2013).

The data sample comprises 106 AGNs (redshift $0 \leq z \leq 4.0$) classified as Seyfert 2 (8 objects), Type 2 Quasars (36 objects), High- z Radio Galaxies (61 objects), and radio-quiet type-2 AGNs (1 object). The stellar mass (M_\star) of the AGN host galaxies is in the range of $10 \leq \log(M_\star/M_\odot) \leq 12$. However, for 51/106 galaxies of the sample, M_\star is not available in the literature. The selection criteria adopted require that the objects have been classified as type 2 AGNs by the authors from whom the data were compiled, and have flux measurements of the $\text{C III}\lambda 1909, \text{C IV}\lambda 1549$, and $\text{He II}\lambda 1640$ emission lines. In general, the objects of our sample present Full Width at Half Maximum (FWHM) lower than 1000 km s^{-1} , therefore, a low or negligible contribution of gas heating/ionization by shocks is expected (e.g. Daltabuit & Cox 1972; Dopita & Sutherland 1996). The emission lines are not reddening corrected due to two factors: (i) the line ratios considered have a near wavelength, being minimal the effect of dust on the emission line ratios (e.g. Kraemer et al. 1994) and (ii) only one hydrogen line ($\text{Ly}\alpha$) is measured for most objects.

In Table 1, identification, redshift, values of $\log(C43)$ and $\log(\text{C III}\lambda 1909/\text{C IV}\lambda 1549)$, low frequency radio luminosity measured at 325 MHz (P_{325}) and 1400 MHz (P_{1400}), are listed, when available. In Figure 1, distributions of the AGN type in terms of the redshift are shown. We note that the sample is dominated by high- z radio galaxies ($\sim 57\%$) and type 2 Quasars ($\sim 34\%$) in the range of $1 \leq z \leq 4$.

In addition to the observational data of type 2 AGNs listed in Table 1, we compiled information for 5 objects classified in the literature as possible AGNs at very high z , that is, in the range of $4.4 \leq z \leq 12.5$. The classification of these objects was carried out by the authors from which the data were compiled through UV diagnostic diagrams (e.g. Feltre et al. 2016; Dors et al. 2018) or by the presence of high excitation lines, as, for instance, $[\text{Ne V}]\lambda 3426$ (see Silcock et al. 2024). These very high- z objects were taken into account in the analysis of the results (see below), but not in the

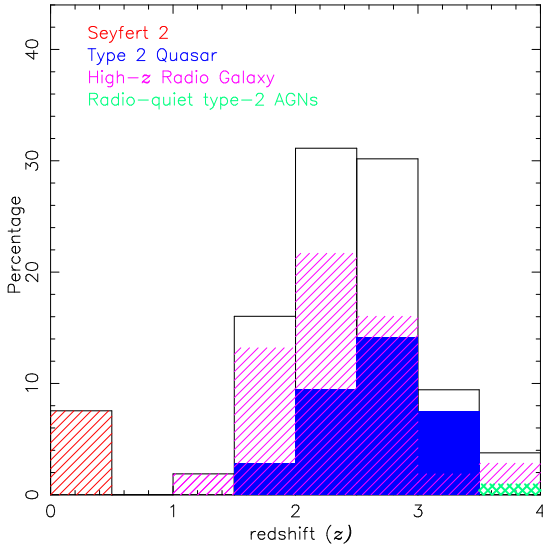


Figure 1. Redshift distribution of the sample of objects (see Table 1) used in the derivation of the new $C43-Z$ calibration. Distribution for the entire sample (106 objects) is represented by black solid line, while distinct AGN classes depicted by different colors, as indicated.

calibration derivation due to the ambiguity of their ionization source (e.g. Bunker et al. 2023). The object identification, redshift, $\log(C43)$ and $\log(C\text{III}]\lambda 1909/\text{C IV}\lambda 1549)$ of this auxiliary sample are listed in Table 2. Again, no reddening correction was performed for these data.

3 RESULTS

Fig. 2 presents diagrams of $\log(C43)$ versus $\log(\text{C III}]/\text{C IV})$, incorporating both the observational data (listed in Table 1) and the results of the photoionization models (see Sect. 2.1) that assume different nebular parameters, as indicated. The models successfully reproduce nearly all of the observational data, depending on the adopted nebular parameters. It should be noted that models with $(Z/Z_\odot) > 1.0$ and $\log U < -2.5$ result in the logarithm of the $C43$ and $\text{C III}]/\text{C IV}$ line ratios overlapping other models with different parameters, making it impossible to derive accurate estimates. This effect arises from a combination of low electron temperatures ($T_e \lesssim 7000$ K) and a reduced number of ionizing photons, resulting in a weak emission line intensities. Consequently, the validity range for nebular parameter estimations based on our calibrations is defined as $0.1 \lesssim (Z/Z_\odot) \lesssim 4.0$ and $-2.5 \lesssim \log U \lesssim -1.0$.

Following Carvalho et al. (2020), who derived a semi-empirical calibration for NLRs based on the relation between $N2 = [\text{N II}]\lambda 6584/\text{H}\alpha$ and Z , we interpolated the model results in each diagram of Fig. 2 (for a similar methodology, see Nagao et al. 2006b; Matsuoka et al. 2009, 2018; Dors et al. 2013, 2021; Castro et al. 2017; Guo et al. 2020; Krabbe et al. 2021; Brinchmann 2023) deriving for each object, when possible, sets of $(Z/Z_\odot, \log U)$ and their corresponding $[\log(C43), \log(\text{C III}]/\text{C IV})]$ values. These types of diagrams (e.g., Fig. 2) combine line ratios that mainly depend on Z (e.g., $C43, R_{23}$) with those that primarily depend on the ionization degree (e.g., $\text{C III}]/\text{C IV}, [\text{O III}]/[\text{O II}]$), thereby mitigating the effect of the ionization parameter on Z estimates, and vice versa (e.g., McGaugh 1991; Dors et al. 2011; Sanders et al. 2016; Oliveira et al. 2024).

In Table 1, the mean values for metallicity [$\langle (Z/Z_\odot) \rangle$] and

ionization parameter ($\langle \log U \rangle$) calculated from the inferred values for each object in the panels of Fig. 2 are listed. The uncertainties of these parameters were calculated by propagating the individual errors derived for each object from the model interpolations (see also Dors et al. 2021). In general, the uncertainties are of the order of $\sim 10 - 20\%$ in Z estimates, reaching up to about 50% for few cases, and ~ 0.1 dex in $\log U$ (see also Table 1 in Dors et al. 2019). In Fig. 3, upper panel, the resulting semi-empirical calibration derived by using the values listed in Table 1 is presented, whose fitting to the points results in

$$(Z/Z_\odot) = (1.114 \pm 0.305) \times w^2 + (2.443 \pm 0.536) \times wy + (1.015 \pm 0.286) \times w + (4.167 \pm 0.206) \times y - (0.928 \pm 0.110), \quad (6)$$

where $w = \log(\text{C III}]\lambda 1909/\text{C IV}\lambda 1549)$ and $y = \log(C43)$. This calibration is valid for the line ratio intervals: $0.0 \lesssim \log(C43) \lesssim 1.2$ and $-1.0 \lesssim \log(\text{C III}]/\text{C IV}) \lesssim 1.0$. In the same direction, we use the interpolated values from Fig. 2 and derived a calibration for $\log U$ in terms of $w = \log(\text{C III}]/\text{C IV})$, given by

$$\log U = (-1.021 \pm 0.025) \times w - (2.282 \pm 0.010) \quad (7)$$

and represented in the lower panel of Fig. 3 by the red line.

4 DISCUSSION

4.1 Comparison with other calibrations

Recently, metallicity and element abundance (O/H, Ne/H, S/H, Ar/H, C/H) estimates have been conducted using the T_e -method for a relatively large sample of AGNs, comprising approximately 150 objects (see, e.g., Flury & Moran 2020; Dors et al. 2020b, 2022, 2023, 2024b, 2025; Armah et al. 2021; Monteiro & Dors 2021; Ji et al. 2024). In particular, Dors et al. (2025) derived, for the first time using the T_e -method, a C/O–O/H relation (i.e. Eq. 5) representative of NLRs. This new relation was obtained by combining direct estimates from both SFs and AGNs, following a method similar to that developed for other elements (e.g. Flury & Moran 2020; Monteiro & Dors 2021; Armah et al. 2021; Dors et al. 2023, 2024b). The use of this abundance relation in photoionization models yields, in principle, more reliable Z calibrations for AGNs based on carbon lines, compared to those relying on other abundance relations that assume SF (e.g. Nakajima & Maiolino 2022) and stellar (e.g. Zhu et al. 2024) abundances or fixed C/O values (e.g. Nagao et al. 2006b; Feltre et al. 2016; Dors et al. 2014, 2019).

As usual, any new calibration must be compared with previous calibrations (e.g., Zhu et al. 2024). Thus, we compare the metallicity estimates from our new calibration (Eq. 6) with those derived from other UV and optical calibrations. A detailed description of the calibrations used in this comparison is presented by Dors et al. (2020a, 2025) and a summary is provided in Table 3. In addition, we compare the Z values obtained via our $C43-Z$ calibration with those derived from the T_e -method. Due to the requirement [e.g. $(S/N) \gtrsim 2$] for reliable measurements of auroral lines (e.g., $[\text{O III}]\lambda 4363$), this comparison was performed only for the six nearby Seyfert 2 galaxies in our sample. Regarding the application of the optical calibrations, the comparison was possible for only a few (6 through the T_e -method and 7 through the N_2 or R_{23} indexes) objects in our sample. The optical emission line intensities (not shown) used in the estimates obtained using the T_e -method and from optical calibrations were taken from Dors et al. (2025). For the UV calibrations, we used the emission-line intensity ratios listed in Table 1.

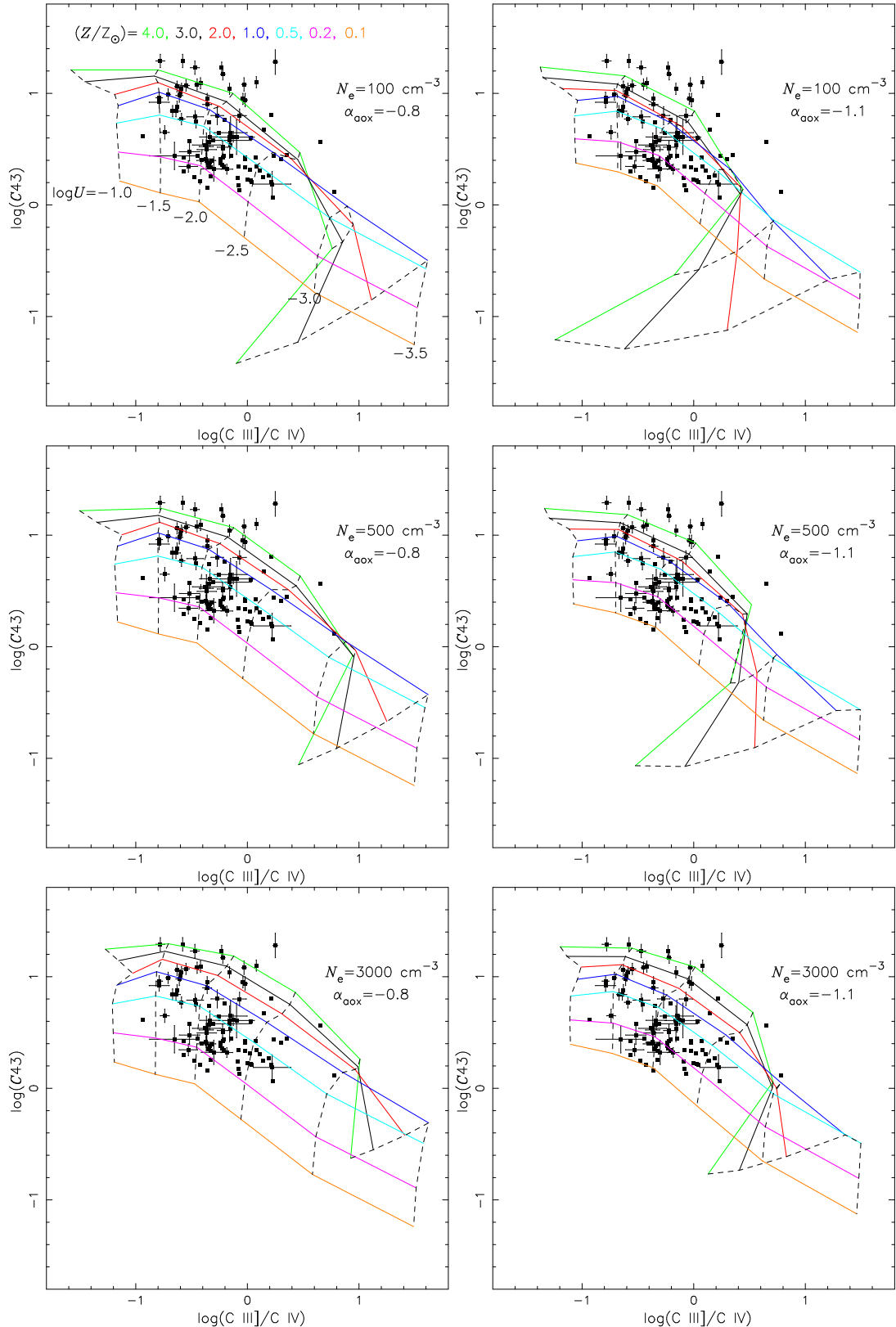


Figure 2. $C_{43} = (\text{C IV}, \lambda 1549 + \text{C III}], \lambda 1909)/\text{He II}, \lambda 1640$ versus $\text{C III}], \lambda 1909/\text{C IV}, \lambda 1549$. Points represent observational narrow emission-line intensity ratios listed in Table 1. Solid lines connect photoionization model results (see Sect. 2.1) with same metallicity, as indicated in the left upper panel. Dashed lines connect models with same ionization parameter as indicated in the left upper panel. In each panel, a grid of models assuming different α_{ox} (as defined in Eq. 1) and electron density (N_e) values, are shown.

Table 1. Sample of objects compiled from the literature by Dors et al. (2014, 2019) and used to obtain the new semi-empirical C43-Z calibration. Identification, redshift (z), $\log(C43) = \log[(C\text{ IV}\lambda1549 + C\text{ IIII}\lambda1909)/\text{He II}\lambda1640]$, $\log(\text{C IIII}\lambda1909/\text{C IV}\lambda1549)$, logarithm of the stellar mass of the host galaxy (in terms of M_\odot), mean metallicity ($< Z/Z_\odot >$) and ionization parameter ($< \log U >$) values derived from the photoionization model result interpolations (Fig. 2), luminosities of Ly α , P_{325} and P_{1400} (see text) are listed when available. Reference from which the radio luminosity values were obtained.

Object	z	$\log(C43)$	$\log(\text{C IIII}/\text{C IV})$	$\log(M_\star)$	$< Z/Z_\odot >$	$< \log U >$	$\log(\text{Ly}\alpha)$	$\log(P_{325})$	$\log(P_{1400})$	Refs.
Seyfert 2										
NGC 1068	0.004	0.60 ± 0.08	-0.33 ± 0.09	—	0.40 ± 0.03	-2.00 ± 0.06	41.43	—	30.26	1, 2
NGC 4507	0.012	0.53 ± 0.10	-0.36 ± 0.12	—	0.32 ± 0.04	-1.98 ± 0.05	41.41	—	29.36	1, 3
NGC 5506	0.006	0.60 ± 0.15	-0.09 ± 0.15	—	0.71 ± 0.07	-2.21 ± 0.07	—	—	29.46	1, 4
NGC 7674	0.029	0.57 ± 0.15	-0.15 ± 0.19	—	0.50 ± 0.07	-2.17 ± 0.08	41.98	—	30.66	1, 2
Mrk 3	0.014	0.52 ± 0.05	-0.36 ± 0.06	—	0.31 ± 0.04	-1.98 ± 0.05	41.48	31.14	30.71	1, 2
Mrk 573	0.017	0.47 ± 0.08	-0.51 ± 0.09	—	0.23 ± 0.05	-1.81 ± 0.08	42.02	—	29.22	1, 2
Mrk 1388	0.021	0.49 ± 0.08	-0.36 ± 0.08	—	0.28 ± 0.05	-1.99 ± 0.05	—	—	29.02	1, 3
MCG-3-34-64	0.017	0.32 ± 0.10	-0.30 ± 0.11	—	0.20 ± 0.04	-2.09 ± 0.06	41.59	—	30.28	1, 4
Type 2 Quasar										
CDFS-031	1.603	0.41 ± 0.04	0.41 ± 0.04	11.43	1.45 ± 0.46	-2.64 ± 0.11	—	—	—	1
CDFS-057	2.562	0.61 ± 0.04	0.61 ± 0.04	10.67	—	—	42.79	—	—	1
CDFS-112a	2.940	0.34 ± 0.05	0.34 ± 0.05	—	0.82 ± 0.07	-2.59 ± 0.08	42.65	—	—	1
CDFS-153	1.536	0.80 ± 0.08	0.80 ± 0.08	—	—	—	—	—	—	1
CDFS-531	1.544	0.32 ± 0.04	0.32 ± 0.04	11.70	0.74 ± 0.07	-2.62 ± 0.03	—	—	—	1
CXO 52	3.288	0.51 ± 0.05	0.51 ± 0.05	—	1.97	-2.63	43.28	—	—	1
015307.0	2.33	1.01 ± 0.05	-0.60 ± 0.01	—	1.74 ± 0.48	-1.60 ± 0.06	44.41	—	—	5
012403.3	2.60	1.06 ± 0.05	-0.63 ± 0.02	—	2.16 ± 0.56	-1.57 ± 0.05	44.82	—	—	5
0130202.4	2.64	0.95 ± 0.05	-0.04 ± 0.02	—	3.24 ± 0.63	-2.05 ± 0.08	44.52	—	—	5
362507.4	2.87	0.88 ± 0.05	-0.63 ± 0.01	—	0.78 ± 0.07	-1.60 ± 0.07	44.82	—	—	5
111507.9	2.81	0.98 ± 0.06	-0.61 ± 0.03	—	1.40 ± 0.40	-1.60 ± 0.07	44.73	—	—	5
344832.1	2.55	1.08 ± 0.05	-0.45 ± 0.02	—	2.97 ± 0.65	-1.72 ± 0.07	44.55	—	—	5
450432.4	2.45	0.99 ± 0.05	-0.71 ± 0.02	—	1.10 ± 0.18	-1.51 ± 0.04	44.84	—	—	5
382532.3	2.73	1.17 ± 0.05	-0.22 ± 0.02	—	3.66	-1.92	44.64	—	—	5
031128.9	2.69	1.07 ± 0.05	-0.55 ± 0.03	—	2.66 ± 0.66	-1.64 ± 0.06	44.61	—	—	5
341538.0	2.40	0.77 ± 0.05	-0.59 ± 0.03	—	0.49	± 0.03	-1.68 ± 0.08	44.48	—	5
401318.4	3.30	0.96 ± 0.05	-0.79 ± 0.03	—	0.90	± 0.05	-1.44 ± 0.07	44.84	—	5
060027.4	2.27	0.84 ± 0.05	-0.64 ± 0.04	—	0.62	± 0.07	-1.62 ± 0.06	44.50	—	5
072950.6	3.15	0.90 ± 0.05	-0.36 ± 0.04	—	1.64	± 0.69	-1.87 ± 0.10	44.89	—	5
074309.0	3.32	0.84 ± 0.05	-0.67 ± 0.02	—	0.59	± 0.08	-1.58 ± 0.06	45.13	—	5
322649.6	2.71	1.29 ± 0.06	-0.58 ± 0.01	—	—	—	44.62	—	—	5
190534.8	2.54	1.04 ± 0.05	-0.59 ± 0.01	—	2.12 ± 0.58	-1.60 ± 0.06	44.98	—	—	5
260321.5	2.28	0.65 ± 0.06	-0.74 ± 0.04	—	0.33	± 0.05	-1.50 ± 0.06	44.46	—	5
233734.8	2.39	1.04 ± 0.05	-0.16 ± 0.01	—	3.18 ± 0.46	-1.97 ± 0.07	44.67	—	—	5
261026.2	3.07	1.10 ± 0.05	0.08 ± 0.01	—	—	—	44.83	—	—	5
005540.5	2.37	1.09 ± 0.05	-0.42 ± 0.01	—	3.16 ± 0.66	-1.74 ± 0.07	44.63	—	—	5
004550.5	2.72	0.75 ± 0.06	-0.46 ± 0.01	—	0.52 ± 0.04	-1.85 ± 0.07	44.21	—	—	5
023258.8	2.90	0.80 ± 0.06	-0.07 ± 0.06	—	2.21 ± 0.69	-2.07 ± 0.08	44.24	—	—	5
035715.5	2.22	1.08 ± 0.06	-0.03 ± 0.02	—	3.76 ± 0.15	-2.04 ± 0.10	44.34	—	—	5
000543.6	2.46	1.28 ± 0.11	0.25 ± 0.02	—	—	—	44.12	—	—	5
015218.3	3.18	1.23 ± 0.06	-0.47 ± 0.04	—	3.66	-1.70	44.03	—	—	5
121119.9	3.14	1.23 ± 0.05	-0.23 ± 0.01	—	—	—	44.67	—	—	5
073116.0	3.05	1.29 ± 0.06	-0.78 ± 0.04	—	—	—	44.69	—	—	5
000848.4	2.22	0.92 ± 0.05	-0.79 ± 0.09	—	0.78 ± 0.05	-1.44 ± 0.07	44.14	—	—	5
010403.3	2.66	0.94 ± 0.06	-0.02 ± 0.02	—	3.26 ± 0.62	-2.07 ± 0.08	44.45	—	—	5
033833.5	2.76	0.95 ± 0.05	-0.36 ± 0.01	—	2.17 ± 0.73	-1.83 ± 0.09	44.42	—	—	5
High- z Radio Galaxy										
USS 1545-234	2.751	0.34 ± 0.01	-0.34 ± 0.02	—	0.19 ± 0.04	-2.04 ± 0.06	—	35.92	35.24	6, 7
USS 2202+128	2.705	0.53 ± 0.01	-0.38 ± 0.01	11.62	0.31 ± 0.04	-1.96 ± 0.06	—	35.79	35.10	6, 7
USS 0003-19	1.541	0.37	-0.23	—	0.25 ± 0.07	-2.15 ± 0.06	—	35.23	34.48	7
MG 0018+0940	1.586	0.60	0.03	—	1.38 ± 0.08	-2.26 ± 0.11	—	35.36	34.84	7
MG 0046+1102	1.813	0.42	0.07	—	0.53 ± 0.05	-2.42 ± 0.05	—	35.42	34.79	7
MG 0122+1923	1.595	0.22	0.00	—	0.29 ± 0.05	-2.42 ± 0.05	—	35.24	34.77	7
USS 0200+015	2.229	0.40	-0.02	—	0.42 ± 0.03	-2.34 ± 0.06	—	35.72	34.97	7
USS 0211-122	2.336	0.40	-0.40	< 11.16	0.21 ± 0.04	-1.96 ± 0.07	43.40	35.94	35.21	7
USS 0214+183	2.130	0.42	-0.22	—	0.30 ± 0.05	-2.15 ± 0.05	—	35.71	35.04	7
MG 0311+1532	1.986	0.43	-0.20	—	0.33 ± 0.05	-2.16 ± 0.05	—	35.37	34.81	7

Table 1. -continued

Object	redshift	$\log(C43)$	$\log(\text{CIII}/\text{CIV})$	$\log(\frac{M_\star}{M_\odot})$	$< Z/Z_\odot >$	$< \log U >$	$\log(\text{Ly}\alpha)$	$\log(P_{325})$	$\log(P_{1400})$	Refs.
High-z Radio Galaxy										
TNJ0121+1320	3.517	0.21 ± 0.02	0.03 ± 0.01	11.02	0.30 ± 0.05	-2.45 ± 0.04	—	35.83	34.97	6, 7
TNJ0205+2242	3.507	0.39 ± 0.04	-0.31 ± 0.05	10.82	0.23 ± 0.06	-2.07 ± 0.05	—	35.88	35.01	6, 7
MRC0316-257	3.130	0.30 ± 0.02	0.11 ± 0.02	11.20	0.42 ± 0.02	-2.49 ± 0.04	—	—	—	6, 7
USS0417-181	2.773	0.26 ± 0.03	0.19 ± 0.04	—	0.44 ± 0.01	-2.57 ± 0.02	—	36.17	35.39	6, 7
TNJ0920-0712	2.758	0.41 ± 0.01	-0.23 ± 0.01	—	0.29 ± 0.06	-2.14 ± 0.05	—	36.00	35.05	6, 7
WNJ1123+3141	3.221	0.61 ± 0.01	-0.93 ± 0.06	< 11.72	0.27 ± 0.05	-1.26 ± 0.07	—	35.99	35.06	6, 7
4C 24.28	2.913	0.32 ± 0.01	-0.18 ± 0.02	< 11.11	0.25 ± 0.06	-2.21 ± 0.05	—	—	—	6, 7
BRL0310-150	1.769	0.57	-0.30	—	0.38 ± 0.05	-2.04 ± 0.04	—	36.12	35.60	7
USS0355-037	2.153	0.13	-0.06	—	0.20 ± 0.03	-2.38 ± 0.05	43.60	35.77	34.99	7
USS0448+091	2.037	0.44	0.35	—	1.32 ± 0.44	-2.58 ± 0.10	43.58	35.31	34.64	7
USS0529-549	2.575	0.56	0.65	11.46	—	—	43.61	—	—	7
4C +41.17	3.792	0.60	-0.16	11.39	0.56 ± 0.07	-2.16 ± 0.06	44.31	36.45	35.66	7
USS0748+134	2.419	0.34	-0.07	—	0.34 ± 0.04	-2.32 ± 0.05	43.48	35.72	34.97	7
USS0828+193	2.572	0.31	0.02	< 11.60	0.37 ± 0.04	-2.41 ± 0.05	43.87	35.55	34.84	7
BRL0851-142	2.468	0.33	-0.32	—	0.20 ± 0.04	-2.07 ± 0.05	—	36.00	35.47	7
TNJ0941-1628	1.644	0.76	-0.20	—	1.10 ± 0.48	-2.04 ± 0.08	—	35.71	34.87	7
USS0943-242	2.923	0.36	-0.22	11.22	0.25 ± 0.06	-2.16 ± 0.05	44.18	36.10	35.36	7
MG1019+0534	2.765	0.25	-0.32	11.15	0.16 ± 0.03	-2.07 ± 0.05	42.74	35.66	35.19	7
TNJ1033-1339	2.427	0.57	-0.51	—	0.31 ± 0.05	-1.80 ± 0.07	43.67	35.89	35.02	7
TNJ1102-1651	2.111	0.20	0.04	—	0.29 ± 0.04	-2.47 ± 0.04	42.97	35.57	34.72	7
USS1113-178	2.239	0.80	0.21	—	2.58	-2.37	43.40	35.72	35.08	7
3C 256.0	1.824	0.24	-0.08	—	0.25 ± 0.05	-2.34 ± 0.05	44.11	36.15	35.51	7
USS1138-262	2.156	0.20	0.21	< 12.11	0.40 ± 0.02	-2.59 ± 0.02	43.70	36.34	35.57	7
BRL1140-114	1.935	0.50	-0.22	—	0.37 ± 0.05	-2.12 ± 0.06	—	36.30	35.60	7
4C 26.38	2.608	0.29	-0.56	—	0.14 ± 0.03	-1.75 ± 0.07	—	—	—	7
MG1251+1104	2.322	0.43	0.23	—	0.84 ± 0.08	-2.51 ± 0.05	43.00	—	—	7
WNJ1338+3532	2.769	0.06	0.22	—	0.30 ± 0.03	-2.63 ± 0.02	44.07	35.72	34.97	7
MG1401+0921	2.093	0.17	-0.08	—	0.21 ± 0.04	-2.35 ± 0.04	—	35.53	34.92	7
3C 294	1.786	0.34	0.07	11.36	0.43 ± 0.03	-2.45 ± 0.05	44.55	—	—	7
USS1410-001	2.363	0.24	-0.47	< 11.41	0.13 ± 0.03	-1.88 ± 0.07	44.10	35.65	35.00	7
USS1425-148	2.349	0.15	-0.36	—	0.15 ± 0.02	-2.08 ± 0.02	43.96	35.65	35.00	7
USS1436+157	2.538	0.64	-0.25	—	0.50 ± 0.07	-2.09 ± 0.05	44.35	—	—	7
3C 324.0	1.208	0.42	-0.02	—	0.44 ± 0.03	-2.34 ± 0.06	—	35.92	35.34	7
USS1558-003	2.527	0.36	-0.35	< 11.70	0.20 ± 0.04	-2.03 ± 0.06	43.90	—	—	7
BRL1602-174	2.043	0.42	-0.56	—	0.19 ± 0.03	-1.75 ± 0.08	—	36.32	35.67	7
TXSJ1650+0955	2.510	0.21	-0.42	—	0.13 ± 0.03	-1.95 ± 0.07	44.04	—	—	7
8C 1803+661	1.610	0.44	-0.44	—	0.22 ± 0.04	-1.91 ± 0.08	—	34.55	33.93	7
4C 40.36	2.265	0.33	-0.02	11.29	0.36 ± 0.04	-2.37 ± 0.05	—	36.24	35.42	7
BRL1859-235	1.430	0.24	0.14	—	0.39 ± 0.02	-2.53 ± 0.04	—	36.29	35.68	7
4C 48.48	2.343	0.38	-0.33	—	0.22 ± 0.05	-2.05 ± 0.06	—	35.87	35.20	7
MRC2025-218	2.630	0.67	0.14	< 11.62	1.78 ± 0.36	-2.32 ± 0.08	43.37	35.89	35.25	7
TXSJ2036+0256	2.130	0.41	0.30	—	1.24 ± 0.79	-2.53 ± 0.10	43.38	35.86	35.09	7
MRC2104-242	2.491	0.53	-0.15	11.19	0.44 ± 0.04	-2.18 ± 0.06	44.46	36.26	35.41	7
4C 23.56	2.483	0.34	-0.21	11.59	0.25 ± 0.06	-2.18 ± 0.06	43.61	—	—	7
MG2121+1839	1.860	0.74	-0.34	—	0.64 ± 0.06	-1.97 ± 0.06	—	35.32	34.73	7
USS2251-089	1.986	0.56	-0.34	—	0.36 ± 0.04	-2.00 ± 0.04	—	35.66	35.07	7
MG2308+0336	2.457	0.44	-0.14	—	0.37 ± 0.05	-2.22 ± 0.06	43.16	35.89	35.32	7
4C 28.58	2.891	0.11	0.77	11.36	0.90 ± 0.06	-2.94 ± 0.03	—	36.30	35.44	7
MP J0340-6507	2.289	0.18 ± 0.11	0.22 ± 0.16	—	0.39 ± 0.02	-2.60 ± 0.02	42.22	—	—	8
TNJ1941-1951	2.667	0.43 ± 0.12	-0.65 ± 0.22	—	0.18 ± 0.03	-1.62 ± 0.08	43.35	—	—	8
MP J2352-6154	1.573	0.39 ± 0.06	-0.36 ± 0.08	—	0.21 ± 0.05	-2.01 ± 0.06	—	—	—	8
Radio-quiet type-2 AGNs										
COSMOS 05162	3.524	0.78 ± 0.05	-0.46 ± 0.07	10.50	0.62 ± 0.08	-1.84 ± 0.08	43.96	—	—	9

References— (1) Nagao et al. (2006b), (2) Condon et al. (2002), (3) Condon et al. (1998), (4) Allison et al. (2014), (5) Silva et al. (2020), (6) Matsuoka et al. (2009), (7) De Breuck et al. (2000), (8) Bornancini et al. (2007), (9) Matsuoka et al. (2018).

Table 2. Sample of very high- z objects classified as AGNs. Emission line ratios are not reddening corrected and were compiled from the literature, as indicated. These data were not included in the derivation of the calibration (see Fig. 3) but were included as auxiliary data along the analysis. Metallicity and ionization parameter were derived by using calibrations represented by Eqs. 6 and 7, respectively.

Object	redshift	$\log(C43)$	$\log(\text{C III]}/\text{C IV})$	Z/Z_{\odot}	$\log U$	Reference
106462	8.51	0.33	-0.14	0.21	-2.13	Treiber et al. (2024)
A744-45924	4.47	1.11	0.38	> 4	-2.66	Labbe et al. (2024)
GHZ2	12.33	1.11	-0.45	2.24	-1.82	Castellano et al. (2024)
GN-z11	10.60	0.56	0.33	2.31	-2.61	Bunker et al. (2023)
GS-3073	5.55	0.39	0.31	1.41	-2.59	Ji et al. (2024)

Table 3. Summary of the calibrations used to compare (Fig. 4) with our new $C43$ - Z calibration (Eq. 6). Columns: (1) Reference, (2) metallicity index used as Z tracer, (3) calibration identification (ID) used along the text, (4) Z validity range, (5) type of calibration.

Reference	Index Name	ID	Validity	Type
Dors et al. (2019)	$C43^a$	D19	Ultraviolet $0.3 \lesssim (Z/Z_{\odot}) \lesssim 2.0$	Semi-empirical
Zhu et al. (2024)	$C43^a$	Z24	$0.03 \lesssim (Z/Z_{\odot}) \lesssim 6.5$	Theoretical Optical
Carvalho et al. (2020)	$N2^b$	C20	$0.3 \lesssim (Z/Z_{\odot}) \lesssim 2.0$	Semi-empirical
Dors (2021)	R_{23}^c	D21	$0.3 \lesssim (Z/Z_{\odot}) \lesssim 2.0$	Empirical
Storchi-Bergmann et al. (1998)	$N2^b$	SB98	$0.5 \lesssim (Z/Z_{\odot}) \lesssim 5.0$	Theoretical

^a $C43 = (\text{C IV}\lambda 1549 + \text{C III]}\lambda 1909)/\text{He II}\lambda 1640$; ^b $N2 = [\text{N II}]\lambda 6584/\text{H}\alpha$;

^c $R_{23} = ([\text{O II}]\lambda 3727 + [\text{O III}]\lambda 4959 + \lambda 5007)/\text{H}\beta$

In Fig. 4, panels (a) and (b), the comparison between the Z estimates from the new calibration (Eq. 6) and those from Dors et al. (2019) and Zhu et al. (2024) UV calibrations, respectively, is shown. We can see that the new $C43$ calibration produces, for the high-metallicity regime ($(Z/Z_{\odot}) \gtrsim 0.7$), higher Z values than those derived via the other UV calibrations, while the opposite result is found for the low-metallicity regime. In the upper part of the panels (a) and (b) of Fig. 4, the logarithm of the ratio ZR between the estimates as a function of Z/Z_{\odot} estimated using the present calibration is shown. The mean discrepancies ($\langle ZR \rangle$) are about -0.5 and 0.6 dex for the low and high-metallicity regime, respectively, when compare our estimations with those using the calibration by Dors et al. (2019), while they are about -1.0 and 1.0 for the different metallicity regimes, respectively, when we performed the same comparison using the calibration by Zhu et al. (2024).

Dors et al. (2025) proposed that the above discrepancy is mainly due to the inappropriate C/O–O/H relation assumed in the photoionization models used to derive the calibrations. If this assertion is right, the Z values from this new calibration (Eq. 6) must be closer to those by the direct estimates. In Fig. 4, panel (c), our Z estimates are compared with those obtained using the T_e -method. Although this comparison is only possible for a few (6) objects, a good agreement is found with $\langle ZR \rangle \sim 0.1$ dex, a value similar to the typical uncertainty in direct estimates due to the errors in emission-line measurements (e.g. Kennicutt et al. 2003; Hägele et al. 2008). As an additional test, in panels (d), (e) and (f) of Fig. 4, we compare Z derived from our calibration (Eq. 6) with those obtained via optical calibrations by Carvalho et al. (2020), Dors (2021) and Storchi-Bergmann et al. (1998), respectively. We note very good agreement between our new estimates and those derived using Carvalho et al. (2020) and Dors (2021) calibrations, with $\langle ZR \rangle$ lower than ~ 0.1 dex. The Storchi-Bergmann et al. (1998) calibration results in somewhat higher ($\langle ZR \rangle \sim 0.3$ dex) Z values. This calibration adopts $N2 = [\text{N II}]\lambda 6584/\text{H}\alpha$ as the Z tracer and is based

on photoionization models that assume an old N/O–O/H relation derived for nuclear starbursts (Storchi-Bergmann et al. 1994), which can not necessarily be representative of AGNs (e.g. Flury & Moran 2020; Dors et al. 2024b; Ji et al. 2024). In any case, Z values derived from our new $C43$ calibration are consistent with those derived from the T_e -method and most optical calibrations. It is worth mentioning that a large number of both UV and optical Z estimates will be needed to confirm this result.

4.2 Metallicity implications

4.2.1 Cosmic metallicity evolution

The metallicity evolution of galaxies is connected to several physical processes operating over their lifetimes, such as mergers, interactions, supernova feedback, gas inflow/outflow, and the environment in which these objects are located (e.g., Haynes et al. 1990; Mouhcine et al. 2007; Krabbe et al. 2011; Davé et al. 2011; Robertson et al. 2012; Troncoso et al. 2014; Wu et al. 2017; Ellison et al. 2009; Kobayashi et al. 2023; Wu et al. 2023; Sun et al. 2025). These complex processes have a strong influence on the metallicity evolution of galaxies, producing a large scatter in Z at a given redshift and/or for galaxies with similar mass (e.g., Matsuoka et al. 2018; Pérez-Díaz et al. 2024, 2025; Villar Martín et al. 2024).

Recent galaxy Z estimations performed by Scholtz et al. (2025a) using the JWST showed the existence of star-forming galaxies with metallicity or elemental abundance (e.g. N, C) values higher than those predicted by standard chemical evolution models (see Dors et al. 2024a and references therein). Recent analysis by Rizzuti et al. (2025) showed that the discrepancy between observational estimated and model predicted values of Z and elemental abundances can be attributed to the fact that standard chemical evolution models of galaxies assume inappropriate star formation rates and/or normal (e.g. Salpeter 1955; Kroupa 2001) stellar Initial Mass Function (IMF), being not necessary to assume peculiar nucleosynthesis

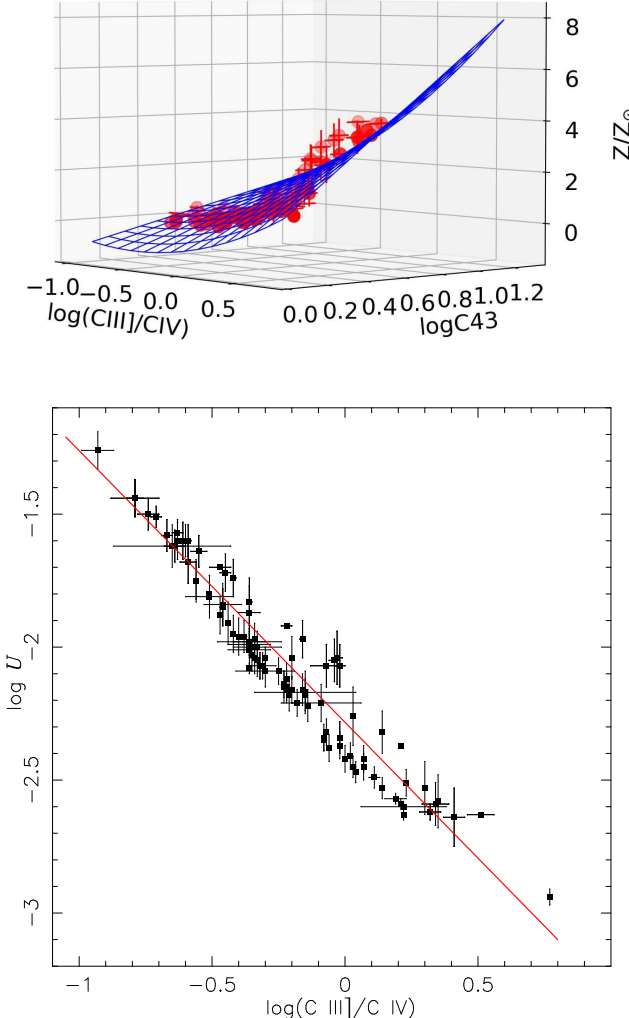


Figure 3. Upper panel: semi-empirical calibration between the metallicity (Z/Z_{\odot}) and the logarithm of the $C43=(C\text{IV}\lambda1549+C\text{III}\lambda1909)/\text{He II}\lambda1640$ and $C\text{III}\lambda1909/\text{C IV}\lambda1549$ line ratios. Points represent our Z/Z_{\odot} estimations (mean values) for the objects in our sample (see Table 1) obtained interpolating our photoionization model results presented in Fig. 2. The surface represents the fitting to the points given by Eq. 6. Lower panel: same as the upper panel but for $\log U$ versus $\log(\text{C III}]\lambda1909/\text{C IV}\lambda1549)$. The line represents the fitting to the points given by Eq. 7.

from population III stars (see also Ji et al. 2025; Gunawardhana et al. 2025; Nakane et al. 2025; Isobe et al. 2025).

Due to the high luminosity of AGNs, most of their narrow and broad emission lines are observed with $(S/N) > 3$, thus permitting the estimation of Z over a wide redshift range (e.g. Nagao et al. 2006a,b; Juarez et al. 2009; Simon & Hamann 2010; Matsuoka et al. 2009; Nagao et al. 2012; Feltre et al. 2016; Thomas et al. 2018; Pérez-Montero et al. 2019; Mignoli et al. 2019; Guo et al. 2020; Pérez-Díaz et al. 2022; do Nascimento et al. 2022; Terao et al. 2022; Carr et al. 2023; Zhu et al. 2024). Our new calibration provides an opportunity to revise the Z evolution in AGNs, particularly in their NLRs. In this context, in Fig. 5, bottom panel, Z estimates for our AGN sample (see Table 1), combined with those for high- z objects (see Table 2), versus redshift are shown. In Fig. 5, middle panel, we present the mean metallicity and redshift values for our sample, where the points represent Z estimates for each class of AGN, as

indicated. Finally, in the upper panel of Fig. 5, we present the cosmic star formation (ψ) history derived by Madau & Dickinson (2014) through ultraviolet and infrared observational data. We can see that:

- The highest Z values (around $\sim 4 Z_{\odot}$) are derived for Type 2 quasars and high- z radio galaxies located in the redshift interval $2 \lesssim z \lesssim 3$. Interestingly, this redshift range is similar to that derived for the maximum value of ψ , according to the results by Madau & Dickinson (2014) (see also Novak et al. 2017; Wang et al. 2024; Gentile et al. 2025; Bosi et al. 2025, among others). This agreement can be due to the possible link among black hole accretion rate (BHAR), star formation rate (SFR) and galaxy stellar mass (M_{\star}), resulting in a strong enrichment of metals in the ISM (e.g. Yang et al. 2017; Zou et al. 2024; Mountrichas & Georgantopoulos 2024). However, we strongly emphasize that the agreement between the maximum Z and ψ values observed in Fig. 5 must be confirmed by additional estimates of Z in AGNs located in a more uniform range of redshifts. Also, Type 2 quasars and High- z radio galaxies usually are hosted in more massive galaxies compared to those of Seyfert 2 nuclei, which could yield an observational bias in the above result, especially if Z_{AGN} is related to the mass of the host galaxy (see below).

- The few possible Z estimates for AGNs observed by the JWST are similar to those for objects in the local universe and at $1.0 \lesssim z \lesssim 4.0$. This result is consistent with that obtained by Nagao et al. (2006b), which indicates that AGNs had already undergone a major episode of metal enrichment in the early ($z > 5$) epoch of the Universe (see also Maiolino et al. 2003; Kurk et al. 2007; Matsuoka et al. 2009; De Rosa et al. 2011, 2014; Schindler et al. 2020; Onoue et al. 2020; Lai et al. 2022; Jiang et al. 2024).

4.2.2 Ionization parameter

The ionization parameter U characterizes the interaction between the ionizing source and the ionized gas (e.g., Sanders et al. 2016) and it represents the degree of excitation of the gas in a given object, reflecting the recombination rate at the face of a cloud exposed to radiation (Peterson 2006). As it is already known, it is defined by

$$U = \frac{Q(H)}{4\pi n(H) r^2 c}, \quad (8)$$

where $Q(H)$ is the number of hydrogen-ionizing photons emitted by the central object, r is the separation [cm] between the center of the ionizing source and the illuminated face of the cloud, $n(H)$ is the total hydrogen density (ionized, neutral, and molecular), and "c" is the speed of light [cm s⁻¹].

Firstly, let us analyze the dependence of U with redshift. Kewley et al. (2013) compared a large sample of SF spectroscopic data ($0.5 < z < 2.6$) with predictions from photoionization models in a $[\text{O III}]/\text{H}\beta$ versus $[\text{N II}]/\text{H}\alpha$ diagnostic diagram. These authors found that the ISM conditions are more extreme at high redshift than in local SFs; i.e., higher U values are expected in high- z SFs compared to local ones (see also Kaasinen et al. 2018; Sanders et al. 2023). However, in relation to AGNs, recent observations from the JADES spectroscopic survey carried out with the JWST by Scholtz et al. (2025b) showed that the 42 identified type 2 AGNs at $z \sim 10$ have a gas ionization degree similar to that found for objects at the local universe (see also Übler et al. 2024; Silcock et al. 2024; Kumari et al. 2024a; Tang et al. 2025; Rinaldi et al. 2025). To study this behavior, in Fig. 6, bottom panel, results of $\log U$ versus redshift for our type 2 AGN sample (see Table 1) and for the auxiliary objects (see Table 2) are shown, separated by AGN classes.

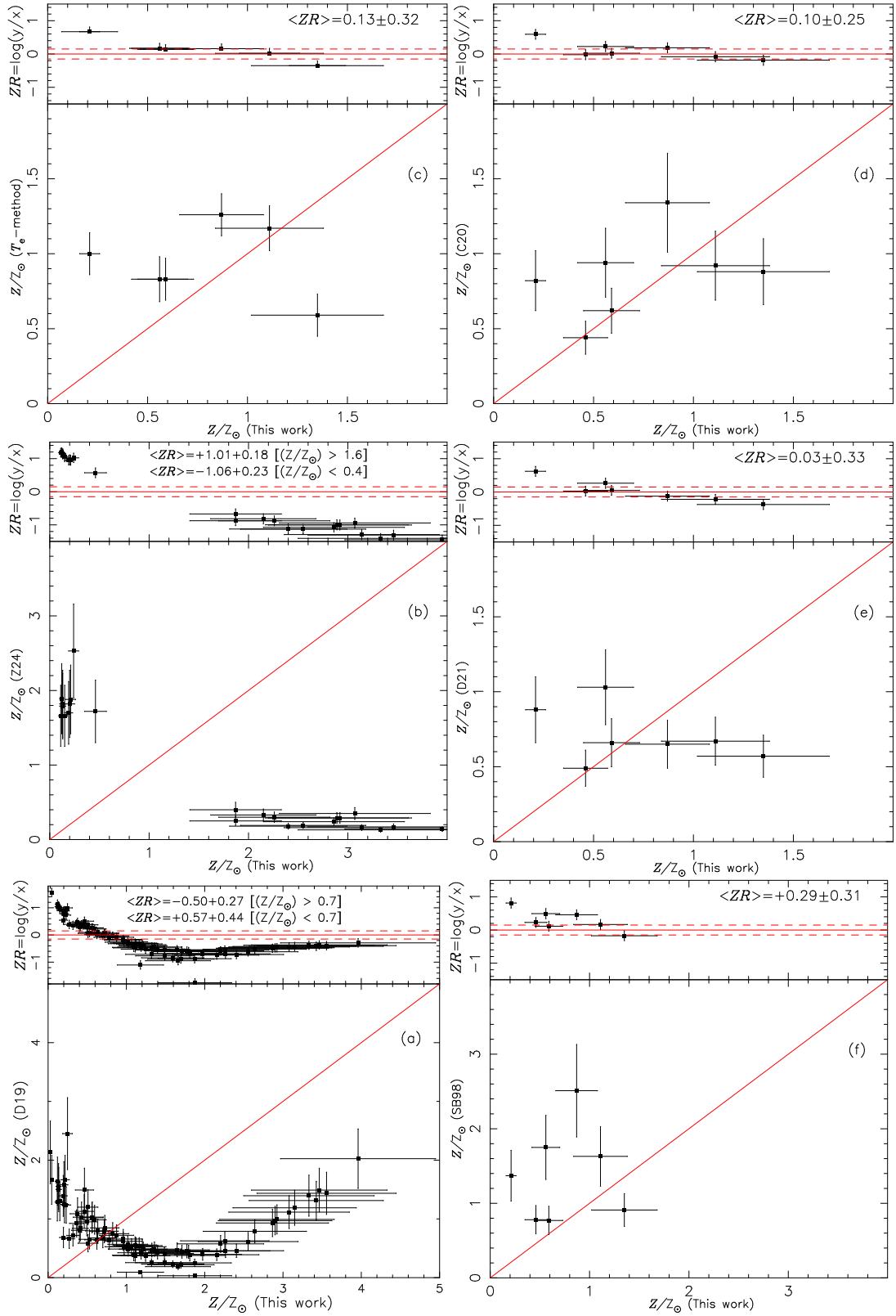


Figure 4. Bottom part of panels: comparison between Z values (in relation to the solar one) derived from our new C43-Z calibration, represented by Eq. 6 and D25, and the ones listed in Table 3. Points represent metallicity estimates for the object in our sample (see Table 1) through distinct calibrations, as indicated. The red lines represent the equality between the estimates. Upper part of panels: logarithm of the ratio between the metallicity estimates (ZR) compared in the bottom part of the corresponding panel versus the estimations from our new C43-Z calibration (Eq. 6). Solid lines represent the equality between the estimates, whilst dashed lines the ratio uncertainty of them. The mean value of ZR is indicated by $\langle ZR \rangle$.

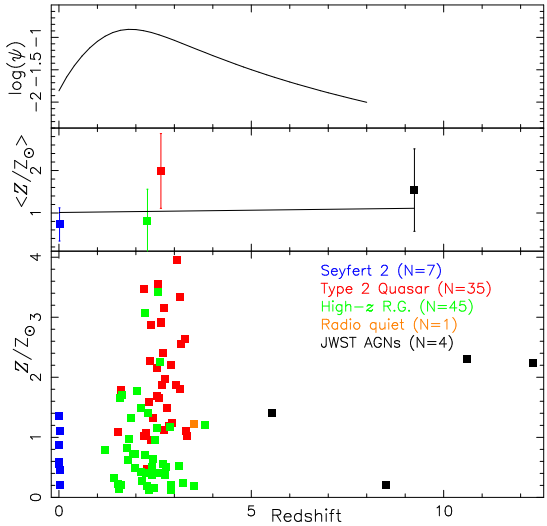


Figure 5. Bottom panel: metallicity (in relation to the solar metallicity value) versus the redshift for the objects in our sample (Table 1). Z values are derived assuming our new $C43-Z$ calibration (Eq. 6). AGN classes are represented by different colors, as indicated. Black point represent JWST estimates for the high- z AGNs listed in Table 2. N represents the number of objects. Middle panel: mean metallicity for the distinct AGN classes versus their mean redshift. The line represents a linear fitting (coefficients not shown) to the points. Upper panel: logarithm of the cosmic star formation (ψ) history derived by Madau & Dickinson (2014).

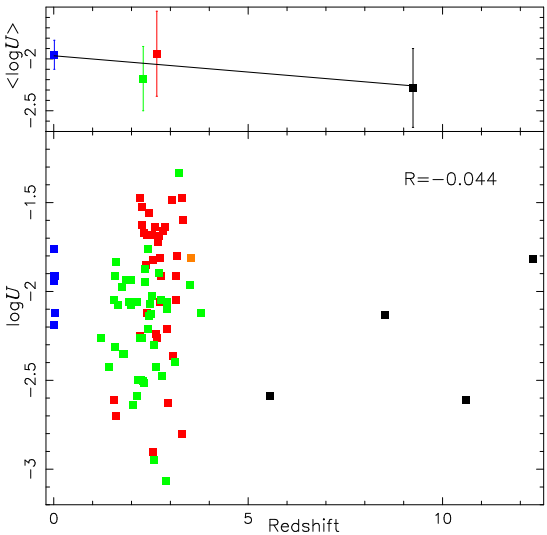


Figure 6. As Fig. 5 but for logarithm of the ionization parameter ($\log U$) estimated using the Eq. 7.

The $\log U$ values were derived using the $([C\text{III}]/\text{CIV})-U$ calibration represented by Eq. 7. We can see a large scattering in U for fixed z values, with a Pearson correlation coefficient $R = -0.044$, i.e. there is no correlation between the estimates. In Fig. 6, upper panel, the mean $\langle \log U \rangle$ parameter for different AGN classes is plotted against z . A trend of slight $\langle \log U \rangle$ decreases with increasing z is observed. A linear fit to all $\langle \log U \rangle$ values results in the following relation:

$$\log U = -0.03(\pm 0.01) \times z - 1.97(\pm 0.09). \quad (9)$$

We emphasize that a large number of AGN estimates in distinct z ranges (e.g. $z \sim 1$ and $z \sim 4$, 'redshift desert') is necessary to confirm the $U-z$ relation derived above.

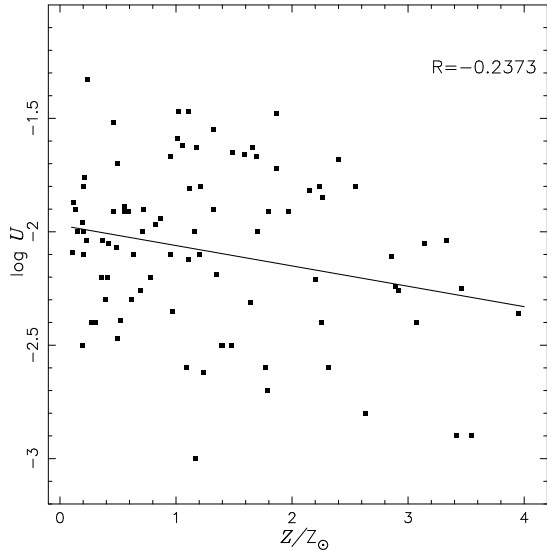


Figure 7. Logarithm of the ionization parameter U versus the metallicity for our AGN sample (see Table 1) derived using the Eqs. 7 and 6, respectively. The line represents a fitting to the points (Eq. 10).

Secondly, we analyze the relation between $\log U$ and Z , for which several studies have shown contradictory results for SFs (e.g., Dors et al. 2011; Sánchez et al. 2015; Onodera et al. 2016; Kashino & Inoue 2019; Papovich et al. 2022; Ji & Yan 2022; Espinosa-Ponce et al. 2022; Reddy et al. 2023; Brinchmann 2023; Pérez-Montero et al. 2024; Garner et al. 2025; Lebouteiller et al. 2025) and AGNs (e.g., Pérez-Montero et al. 2019; Oliveira et al. 2024; Vidal-García et al. 2024), mainly due to the different methods (see Kewley & Ellison 2008; Dors et al. 2020a) adopted to derive these parameters or the used samples. In Fig. 7, a plot of $\log U$ versus Z/Z_{\odot} , our estimates for both object samples (see Tables 1 and 2), derived from the calibrations given by Eqs. 7 and 6, respectively, are shown. Objects are not separated by classes. We can note that $\log U$ tends to decrease with Z , following the relation:

$$\log U = -0.08(\pm 0.03) \times (Z/Z_{\odot}) - 1.97(\pm 0.06). \quad (10)$$

This result is in agreement with the one obtained by Pérez-Montero et al. (2019), who using the HCM code, found for local Seyfert 2 that $\log U$ tend to decrease with increasing Z .

Finally, in Fig. 8, we analyze the dependence between the ionization parameter (U) and the Ly α luminosity for our sample. Again, the ionization parameter values were derived from the $(\text{CIII}/\text{CIV})-\log U$ calibration (Eq. 7), using the observational data listed in Table 1. Despite a large scatter, a (weak) correlation ($R = 0.3312$) can be identified between the quantities, represented by

$$\log(\text{Ly}\alpha)[\text{erg s}^{-1}] = 0.85(\pm 0.29) \times \log U + 45.58(\pm 0.61). \quad (11)$$

From this analysis, we can assert that:

- Most of the AGNs in our sample could be classified as matter-bounded, because an increase in the number of ionizing photons ($U \sim Q(H)$) leads to a direct increase in the Ly α luminosity, or in other words, in the ionized radius of the objects.

- Objects with a high ionization parameter ($\log U \gtrsim -2.0$) and low luminosity ($\log \text{Ly}\alpha \lesssim 42 \text{ erg s}^{-1}$) could have a strong escape of ionizing radiation due to the combined effect of high $Q(H)$ values and low gas content (radiation-bounded).

Both assertions would be confirmed in a future study based on de-

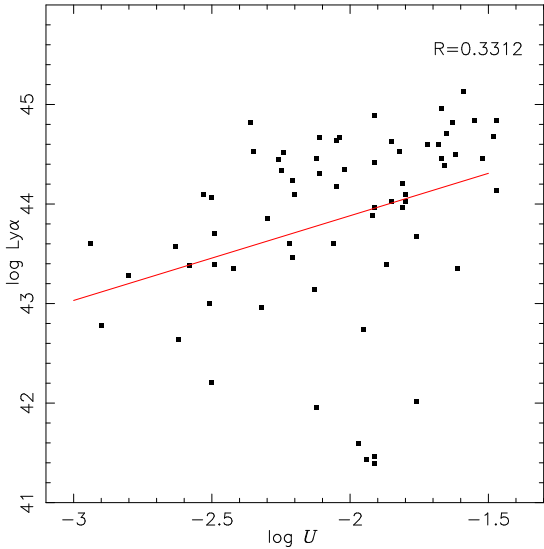


Figure 8. Logarithm of the ionization parameter versus the logarithm of the luminosity of Ly α for our sample of AGNs (see Table 1). Values for log U were derived from Eq. 7. Pearson coefficient correlations (R) is presented in the plot. Red line represents a fitting to the points given by Eq. 11.

tailed photoionization models assuming distinct AGN geometries and gas contents.

4.3 Radio data correlations

Kellermann et al. (1969) presented follow up observations of the Revised Third Cambridge Catalogue (Bennett 1962) and used the flux density (S) at two different frequencies (ν_1, ν_2) as a definition of the spectral index:

$$\alpha_{\nu_1}^{\nu_2} = \frac{\log(S_1/S_2)}{\log(\nu_1/\nu_2)}. \quad (12)$$

Afterward, for example, Condon (1992) showed that distinct object classes (e.g., active and non-active galaxies) present different α values (see also, Niklas et al. 1997; Lisenfeld & Völk 2000; Tabatabaei et al. 2017; de Gasperin et al. 2018, among others).

The correlation between radio indexes and emission line luminosities observed in most of radio galaxies and quasars indicates that the central AGN is the common energy source for both (e.g. McCarthy et al. 1990; Willott et al. 1999) as well as it shows a strong connection between radio emission and conditions in the NLRs (e.g. Kuźmicz & Jamrozy 2021). However, De Breuck et al. (2000) found that UV line ratios are not correlated with radio size or radio power of High- z radio galaxies, with the exception of the C II] $\lambda 2326$ /C III] $\lambda 1909$ ratio, for which there is a correlation only for small radio sources, i.e. $D \lesssim 150$ kpc (see also Inskip et al. 2002). Moreover, Zajaček et al. (2019) found that the location of radio sources in the narrow emission line diagnostic diagrams shifts with the increasing importance of a radio-loudness AGN away from galaxies dominated by radio emission powered by star formation. Thus, this result indicates that the NLR conditions (e.g., U , Z , α_{ox}), which drive the AGN position in BPT diagrams (e.g., Richardson et al. 2014; Feltre et al. 2016), can be related to radio density fluxes. Since our sample is composed mainly (~ 60 per cent) of radio galaxies, it is useful to verify the existence of spectral index correlations with AGN parameters. In this context, we use the

$$\alpha_{325}^{1400} = \frac{\log[P(325 \text{ MHz})/P(1400 \text{ MHz})]}{\log(325 \text{ MHz}/1400 \text{ MHz})} \quad (13)$$

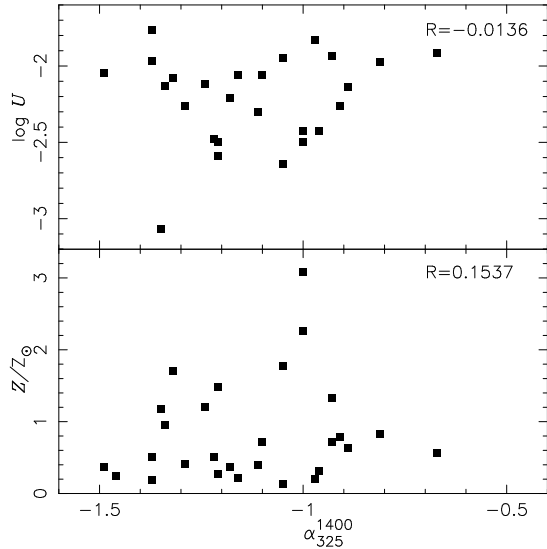


Figure 9. Metallicity (bottom panel) and logarithm of U (upper panel) versus the radio spectral index α_{325}^{1400} index (Eq. 13) for our AGN sample (see Table 1). Z and U were derived from Eq. 6 and 7, respectively. Pearson coefficient correlations (R) are indicated in each panel.

spectral index (using the radio data listed in Table 1) to analyze possible correlations with Z and U . In Fig. 9, metallicity (bottom panel) and the logarithm of the ionization parameter (upper panel) versus the α_{325}^{1400} for our sample of High- z radio galaxies (29 objects) and Seyfert 2 (1 object) are shown. We observe that, in agreement with De Breuck et al. (2000), no correlation was derived, as indicated by the "R" values. Finally, we tested the dependence (not shown) between Z , U and the radio power P_{1400} and did not find any correlation.

4.4 Mass-metallicity relation

The pioneering study by Lequeux et al. (1979) showed a clear and direct relation between the mass of galaxies and their metallicity (i.e. mass-metallicity relation, MZR). This relation arises due to more massive galaxies have deeper gravitational potential wells, which make it much harder for supernova- or AGN-driven winds to expel metals into the intergalactic medium. In contrast, low-mass galaxies lose a larger fraction of their metals through winds, so they tend to exhibit lower Z compared to more massive systems (e.g., Tremonti et al. 2004; Chisholm et al. 2018; Forbes et al. 2019; Sharda et al. 2021).

Regarding the relation between the AGN metallicity (Z_{AGN}) and the host galaxy mass, it could exist if the AGN chemical evolution is connected with that of the entire galaxy in which it is located. However, this relation is debated in the literature, and discrepant results have been derived, which can be due to the methods used to derive Z , the range of galaxy mass, and/or the redshift range of the sample. For instance, Matsuoka et al. (2018), who estimated Z from UV emission lines for a sample of type 2 AGNs ($1.2 < z < 4.0$), showed that there is a direct relation between the NLR metallicities and the stellar masses (M_{\star}) of their host galaxies (see also Dors et al. 2019). However, Dors et al. (2020a), who estimated Z via optical emission lines for a large sample (463 objects) of Seyfert 2 nuclei in the local universe ($z < 0.4$), did not find any relation between Z_{AGN} and M_{\star} of the host galaxy, independent of the method used to derive the metallicity (see also Oliveira et al. 2024; Li et al. 2024b).

Since our new C43-Z calibration provides reliable values, i.e., in agreement with those obtained via the T_e method, it is desirable to in-

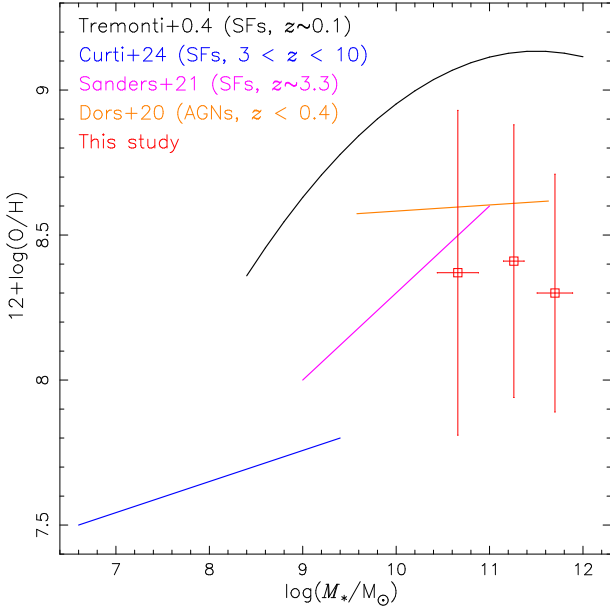


Figure 10. Metallicity (traced by O/H abundance) of the NLR for our AGN sample (see Table 1) versus the logarithm of stellar mass of the host galaxy (in units of solar mass). Red open squares represent mean metallicity for our sample derived considering estimates via our calibration (Eq. 6). Solid curves represent the relations for SF galaxies at distinct redshift and mass ranges by Tremonti et al. (2004), Sanders et al. (2021) and Curti et al. (2024) as indicated. Also, the relation for local ($z < 0.4$) AGNs derived using observational data by Dors et al. (2020a), whose Z_{AGN} was derived applying the empirical calibration by Dors (2021) is indicated.

vestigate the $Z_{\text{AGN}}-M_{\star}$ relation for the sample of objects considered in the present study. In this context, we divide the sample into bins of 0.5 dex for the stellar mass ($10.67 \lesssim \log(\frac{M_{\star}}{M_{\odot}}) \lesssim 11.7$) and calculate the mean value of Z . For a total of 18 objects ($1.5 < z < 3.6$) in our sample, it was possible to consider estimates for Z_{AGN} and M_{\star} . This reduced number is due to the lack of M_{\star} combined with the valid range of Z defined by our metallicity calibration (see Table 1). In Fig. 10, a plot of $12+\log(\text{O/H})^1$ versus $\log(M_{\star}/M_{\odot})$, shows the results for our estimates (red open squares). For comparison, we also plot several mass–metallicity relations from the literature:

- The mass–metallicity relation for ~ 53000 SF galaxies ($z \sim 0.1$) derived by Tremonti et al. (2004) and valid for $8.5 < \log(M_{\star}/M_{\odot}) < 11.5$. These authors used strong-line methods to estimate Z .
- The mass–metallicity relation derived by Curti et al. (2024) for SF galaxies at $3 < z < 10$ and with $\log(M_{\star}/M_{\odot}) \lesssim 9$. The Z values were estimated through strong-line methods.
- The mass–metallicity relation derived by Sanders et al. (2021) for SF galaxies at $z \sim 3.3$ by using Z estimates from strong-line methods. The mass interval considered by these authors is $9 < \log(M_{\star}/M_{\odot}) < 10.5$.
- The $M_{\star}-Z_{\text{AGN}}$ derived using spectroscopic data by Dors et al. (2020a) for ~ 400 AGNs at $z < 0.4$. The Z_{AGN} for each object was derived through the R_{23} –(O/H) empirical calibration proposed by Dors (2021). This derived relation is valid for $9.5 < \log(M_{\star}/M_{\odot}) < 11.5$.

¹ We convert metallicity into O/H abundance by the expression $12 + \log(\text{O/H}) = 12 + \log[(Z/Z_{\odot}) \times 10^{-3.31}]$, where $\log(\text{O/H})_{\odot} = -3.31$ (Allende Prieto et al. 2001).

We can see in Fig. 10 that our $Z_{\text{AGN}}-M_{\star}$ estimations (red open squares) for AGNs at $1.5 < z < 3.6$ is flat, which does not indicate any dependence between the AGN metallicity and M_{\star} . Our results are in agreement with estimations for local ($z < 0.4$) AGNs derived by Dors et al. (2020a). It is worth noting that the AGNs of our sample are located in more massive galaxies than those considered by Curti et al. (2024) and Sanders et al. (2021), while the former studied galaxies in a wider redshift range than the objects in our sample and the last authors only considered objects at $z \sim 3.3$. In both cases, they derived steep relations between Z and M_{\star} . Finally, comparing our estimations with the relation derived by Tremonti et al. (2004), we can see that AGNs have a lower mean metallicity compared to SFs with similar masses. From a galaxy evolution perspective, the flat $Z_{\text{AGN}}-M_{\star}$ relation presented in Fig. 10 is a significant result. It contrasts sharply with the well-established positive MZR for star-forming galaxies, where the deeper gravitational potential wells of more massive galaxies are better able to retain the metals produced by supernovae.

We emphasize that in some previous studies, in which the AGN metallicity is derived from UV emission lines (e.g. Matsuoka et al. 2018; Dors et al. 2019), an increase of Z_{AGN} with M_{\star} has been derived. However, most of those Z estimates were performed using carbon UV emission line intensities and photoionization model predictions assuming a C/O–O/H abundance relation that may not be representative of AGNs. In contrast, in the present study the C/O–O/H relation derived from AGNs and SFs based on the T_{e} -method is assumed in the photoionization models. The sample used in Paper I to constrain the relation for active nuclei included only 7 AGNs. Although this number is small, it represents the first such relation for AGNs derived using the most reliable direct method. Our current work is an application of this new, physically motivated relation to test its implications on a larger sample of objects. We emphasize that refining this C/O–O/H relation with a larger sample of AGNs with direct-method abundances is a critical next step for the field. Nevertheless, the C/O–O/H relation assumed in our models is expected to provide, in principle, more reliable results than those obtained using previous methods (see Dors et al. 2025).

5 CONCLUSION

In a previous study, Dors et al. (2025) (Paper I) used abundance estimates obtained through the T_{e} -method (the most reliable method) to derive a C/O–O/H relation representative for narrow line regions of AGNs. Assuming this abundance relation in a grid of photoionization models and using ultraviolet spectroscopic data (compiled from the literature) of 106 type 2 AGNs ($0 \lesssim z \lesssim 4$), we obtained a new semi-empirical calibration between the $C43=(\text{C IV}\lambda 1549+\text{C III}\lambda 1909)/\text{He II}\lambda 1640$ line ratio and Z for the NLRs of AGNs. A calibration between the $C3C4=(\text{C III}\lambda 1909/\text{C IV}\lambda 1549)$ line ratio and the ionization parameter U was also proposed. Applying these new calibrations we obtain the following results and conclusions:

- Metallicity derived through the new calibration is consistent with those derived through the T_{e} -method and optical strong-line methods. Although the comparison of Z derived by methods based on optical emission lines is possible for few objects, the consistency between the Z values indicate that the new $C43-Z$ calibration results in reliable values.
- Combining auxiliary observational data of AGNs at $5 \lesssim z \lesssim 12$ with those of our sample, we find no evidence for a monotonic evolution of AGN metallicity across the redshift range $0 \lesssim z \lesssim 12$.

This result indicates that AGNs had the main star formation episode and chemical enrichment of the ISM in an early epoch ($z > 5$) of their formation. The most striking feature is the evidence for very high metallicities at all epochs. Notably, the highest metallicities in our sample, reaching up to $4 Z_{\odot}$, are found in luminous Type 2 Quasars and high-redshift radio galaxies at $2 \leq z \leq 3$. As shown in Fig. 5, this epoch coincides with the peak of the cosmic star formation rate history (ψ). This finding strongly suggests a powerful link between the ‘cosmic noon’ of star formation, rapid supermassive black hole growth, and an intense, early chemical enrichment phase in the host galaxies of luminous AGNs.

- We found a slight decrease of the ionization parameter $U \approx Q(\text{H})/N_e$ with the increase of the redshift. This result indicates that either the number of ionization photons decrease with z or AGNs at higher redshifts present higher N_e values compared to those in the local universe ($z < 0.4$).
- We found no significant correlations between radio data [spectral index α_{325}^{1400} and luminosity $L(1400 \text{ MHz})$] and Z , as well as U of the AGNs, which indicates that the central AGN is not the common energy source for ionized and neutral gas regions.

• We find no statistically significant evidence for a positive MZR, and that the data are consistent with a flat relation. The lack of a mass-metallicity dependence for AGNs, both at high redshift (this study) and in the local universe, suggests that the chemical evolution of the gas in the immediate vicinity of the supermassive black hole is decoupled from the global chemical evolution of the host galaxy. We note here that a larger and more homogeneous sample is required to confirm this result.

ACKNOWLEDGEMENTS

OLD is grateful to Fundação de Amparo à Pesquisa do Estado de São Paulo (FAPESP) and Conselho Nacional de Desenvolvimento Científico e Tecnológico (CNPq). MA gratefully acknowledges support from Fundação de Amparo à Pesquisa do Estado de São Paulo (FAPESP, Processo: 2024/03727-3).

DATA AVAILABILITY

The data underlying this article will be shared on reasonable request to the corresponding author.

REFERENCES

- Aannestad P. A., 1989, *ApJ*, **338**, 162
 Alexandroff R., et al., 2013, *MNRAS*, **435**, 3306
 Allende Prieto C., Lambert D. L., Asplund M., 2001, *ApJ*, **556**, L63
 Allison J. R., Sadler E. M., Meekin A. M., 2014, *MNRAS*, **440**, 696
 Arellano-Córdova K. Z., Esteban C., García-Rojas J., Méndez-Delgado J. E., 2020, *MNRAS*, **496**, 1051
 Arevalo Gonzalez F., et al., 2025, arXiv e-prints, p. arXiv:2501.09585
 Armah M., et al., 2021, *MNRAS*, **508**, 371
 Armah M., et al., 2024, *MNRAS*, **534**, 2723
 Bennett A. S., 1962, *Mem. RAS*, **68**, 163
 Berg D. A., Skillman E. D., Croxall K. V., Pogge R. W., Moustakas J., Johnson-Groh M., 2015, *ApJ*, **806**, 16
 Berg D. A., Skillman E. D., Henry R. B. C., Erb D. K., Carigi L., 2016, *ApJ*, **827**, 126
 Berg D. A., et al., 2024, *ApJ*, **971**, 87
 Binette L., et al., 2024, *A&A*, **684**, A53
 Blaes O., 2014, *Space Sci. Rev.*, **183**, 21
 Bornancini C. G., De Breuck C., de Vries W., Croft S., van Breugel W., Röttgering H., Minniti D., 2007, *MNRAS*, **378**, 551
 Bosi M., et al., 2025, *ApJ*, **984**, 117
 Brinchmann J., 2023, *MNRAS*, **525**, 2087
 Brown M. J. I., Duncan K. J., Landt H., Kirk M., Ricci C., Kamraj N., Salvato M., Ananna T., 2019, *MNRAS*, **489**, 3351
 Bundy K., et al., 2015, *ApJ*, **798**, 7
 Bunker A. J., et al., 2023, *A&A*, **677**, A88
 Calabro A., et al., 2023, *A&A*, **679**, A80
 Carniani S., et al., 2024, *Nature*, **633**, 318
 Carr D. J., Salzer J. J., Gronwall C., Williams A. L., 2023, *ApJ*, **955**, 141
 Carvalho S. P., et al., 2020, *MNRAS*, **492**, 5675
 Castellano M., et al., 2024, *ApJ*, **972**, 143
 Castro C. S., Dors O. L., Cardaci M. V., Häggle G. F., 2017, *MNRAS*, **467**, 1507
 Cheng H., Yuan W., Liu H.-Y., Breeveld A. A., Jin C., Liu B., 2019, *MNRAS*, **487**, 3884
 Chisholm J., Tremonti C., Leitherer C., 2018, *MNRAS*, **481**, 1690
 Citro A., Berg D. A., Erb D. K., Auger M. W., Becker G. D., James B. L., Skillman E. D., 2024, *ApJ*, **969**, 148
 Condon J. J., 1992, *ARA&A*, **30**, 575
 Condon J. J., Cotton W. D., Greisen E. W., Yin Q. F., Perley R. A., Taylor G. B., Broderick J. J., 1998, *AJ*, **115**, 1693
 Condon J. J., Cotton W. D., Broderick J. J., 2002, *AJ*, **124**, 675
 Curti M., et al., 2024, *A&A*, **684**, A75
 Czerny B., Elvis M., 1987, *ApJ*, **321**, 305
 D’Silva J. C. J., et al., 2025, arXiv e-prints, p. arXiv:2503.03431
 Daltabuit E., Cox D., 1972, *ApJ*, **173**, L13
 Davé R., Finlator K., Oppenheimer B. D., 2011, *MNRAS*, **416**, 1354
 Davies R., et al., 2020, *MNRAS*, **498**, 4150
 De Breuck C., Röttgering H., Miley G., van Breugel W., Best P., 2000, *A&A*, **362**, 519
 De Rosa G., Decarli R., Walter F., Fan X., Jiang L., Kurk J., Pasquali A., Rix H. W., 2011, *ApJ*, **739**, 56
 De Rosa G., et al., 2014, *ApJ*, **790**, 145
 Díaz Á. I., Terlevich E., Castellanos M., Häggle G. F., 2007, *MNRAS*, **382**, 251
 Dopita M. A., Sutherland R. S., 1996, *ApJS*, **102**, 161
 Dopita M. A., et al., 2006, *ApJS*, **167**, 177
 Dopita M. A., Sutherland R. S., Nicholls D. C., Kewley L. J., Vogt F. P. A., 2013, *ApJS*, **208**, 10
 Dopita M. A., et al., 2015, *ApJS*, **217**, 12
 Dors O. L., 2021, *MNRAS*, **507**, 466
 Dors Jr. O. L., Krabbe A., Häggle G. F., Pérez-Montero E., 2011, *MNRAS*, **415**, 3616
 Dors O. L., et al., 2013, *MNRAS*, **432**, 2512
 Dors O. L., Cardaci M. V., Häggle G. F., Krabbe Á. C., 2014, *MNRAS*, **443**, 1291
 Dors O. L., Agarwal B., Häggle G. F., Cardaci M. V., Rydberg C.-E., Riffel R. A., Oliveira A. S., Krabbe A. C., 2018, *MNRAS*, **479**, 2294
 Dors O. L., Monteiro A. F., Cardaci M. V., Häggle G. F., Krabbe A. C., 2019, *MNRAS*, **486**, 5853
 Dors O. L., et al., 2020a, *MNRAS*, **492**, 468
 Dors O. L., Maiolino R., Cardaci M. V., Häggle G. F., Krabbe A. C., Pérez-Montero E., Armah M., 2020b, *MNRAS*, **496**, 3209
 Dors O. L., Contini M., Riffel R. A., Pérez-Montero E., Krabbe A. C., Cardaci M. V., Häggle G. F., 2021, *MNRAS*, **501**, 1370
 Dors O. L., et al., 2022, *MNRAS*, **514**, 5506
 Dors O. L., et al., 2023, *MNRAS*, **521**, 1969
 Dors O. L., Cardaci M. V., Häggle G. F., Ilha G. S., Oliveira C. B., Riffel R. A., Riffel R., Krabbe A. C., 2024a, *MNRAS*, **527**, 8193
 Dors O. L., et al., 2024b, *MNRAS*, **534**, 3040
 Dors O. L., et al., 2025, *MNRAS*, **540**, 1608
 Duan Q., et al., 2024, arXiv e-prints, p. arXiv:2411.04944
 Durré M., Mould J., 2022, *MNRAS*, **509**, 2377
 Ellison S. L., Simard L., Cowan N. B., Baldry I. K., Patton D. R., McConnachie A. W., 2009, *MNRAS*, **396**, 1257

- Espinosa-Ponce C., Sánchez S. F., Morisset C., Barrera-Ballesteros J. K., Galbany L., García-Benito R., Lacerda E. A. D., Mast D., 2022, *MNRAS*, **512**, 3436
- Esteban C., García-Rojas J., Peimbert M., Peimbert A., Ruiz M. T., Rodríguez M., Carigi L., 2005, *ApJ*, **618**, L95
- Esteban C., Bresolin F., Peimbert M., García-Rojas J., Peimbert A., Mesa-Delgado A., 2009, *ApJ*, **700**, 654
- Esteban C., Bresolin F., García-Rojas J., Toribio San Cipriano L., 2020, *MNRAS*, **491**, 2137
- Feltre A., Charlton S., Gutkin J., 2016, *MNRAS*, **456**, 3354
- Ferland G. J., 1992, *ApJ*, **389**, L63
- Ferland G. J., et al., 2017, *Rev. Mex. Astron. Astrofis.*, **53**, 385
- Flury S. R., Moran E. C., 2020, *MNRAS*, **496**, 2191
- Forbes J. C., Krumholz M. R., Speagle J. S., 2019, *MNRAS*, **487**, 3581
- Freitas I. C., et al., 2018, *MNRAS*, **476**, 2760
- Garner R., Kennicutt R., Rousseau-Nepton L., Olivier G. M., Fernández-Arenas D., Robert C., Martin R. P., Amram P., 2025, *ApJ*, **978**, 70
- Garnett D. R., Dufour R. J., Peimbert M., Torres-Peimbert S., Shields G. A., Skillman E. D., Terlevich E., Terlevich R. J., 1995, *ApJ*, **449**, L77
- Garnett D. R., Shields G. A., Peimbert M., Torres-Peimbert S., Skillman E. D., Dufour R. J., Terlevich E., Terlevich R. J., 1999, *ApJ*, **513**, 168
- Gavilán M., Díaz A. I., Zamora S., 2025, *A&A*, **694**, A61
- Gentile F., et al., 2025, *A&A*, **697**, A46
- Geris S., et al., 2025, arXiv e-prints, p. arXiv:2506.22147
- Groves B. A., Heckman T. M., Kauffmann G., 2006, *MNRAS*, **371**, 1559
- Gunasekara C. M., Ji X., Chatzikos M., Yan R., Ferland G., 2022, *MNRAS*, **512**, 2310
- Gunasekara C. M., Ji X., Chatzikos M., Yan R., Ferland G., 2023, *MNRAS*, **520**, 4345
- Gunawardhana M. L. P., Brinchmann J., Croom S., Bunker A., Bryant J., Oh S., 2025, arXiv e-prints, p. arXiv:2504.12584
- Guo Y., et al., 2020, *ApJ*, **898**, 26
- Gutiérrez E. M., Vieyro F. L., Romero G. E., 2021, *A&A*, **649**, A87
- Hägele G. F., Pérez-Montero E., Díaz Á. I., Terlevich E., Terlevich R., 2006, *MNRAS*, **372**, 293
- Hägele G. F., Díaz Á. I., Terlevich E., Terlevich R., Pérez-Montero E., Cardaci M. V., 2008, *MNRAS*, **383**, 209
- Hamann F., Ferland G., 1992, *ApJ*, **391**, L53
- Hayes M. J., Saldana-Lopez A., Citro A., James B. L., Mingozi M., Scarlata C., Martinez Z., Berg D. A., 2025, *ApJ*, **982**, 14
- Haynes M. P., Herter T., Barton A. S., Benenson J. S., 1990, *AJ*, **99**, 1740
- Hsiao T. Y.-Y., et al., 2024, arXiv e-prints, p. arXiv:2409.04625
- Hu W., et al., 2024, *ApJ*, **971**, 21
- Humphrey A., 2019, *MNRAS*, **486**, 2102
- Ilha G. S., et al., 2022, *MNRAS*, **516**, 1442
- Indriolo N., Geballe T. R., Oka T., McCall B. J., 2007, *ApJ*, **671**, 1736
- Inskip K. J., Best P. N., Rawlings S., Longair M. S., Cotter G., Röttgering H. J. A., Eales S., 2002, *MNRAS*, **337**, 1381
- Isobe Y., et al., 2023, *ApJ*, **959**, 100
- Isobe Y., et al., 2025, arXiv e-prints, p. arXiv:2502.12091
- Jenkins E. B., 2009, *ApJ*, **700**, 1299
- Jensen E. B., Strom K. M., Strom S. E., 1976, *ApJ*, **209**, 748
- Ji X., Yan R., 2022, *A&A*, **659**, A112
- Ji X., et al., 2024, *MNRAS*, **535**, 881
- Ji X., Belokurov V., Maiolino R., Monty S., Isobe Y., Kravtsov A., McClymont W., Übler H., 2025, arXiv e-prints, p. arXiv:2505.12505
- Jiang T., Malhotra S., Rhoads J. E., Yang H., 2019, *ApJ*, **872**, 145
- Jiang D., et al., 2024, *ApJ*, **975**, 214
- Juan de Dios L., Rodríguez M., 2017, *MNRAS*, **469**, 1036
- Juarez Y., Maiolino R., Mujica R., Pedani M., Marinoni S., Nagao T., Marconi A., Oliva E., 2009, *A&A*, **494**, L25
- Juodžbalis I., et al., 2023, *MNRAS*, **525**, 1353
- Juodžbalis I., et al., 2024, *MNRAS*, **535**, 853
- Kaasinen M., Kewley L., Bian F., Groves B., Kashino D., Silverman J., Kartaltepe J., 2018, *MNRAS*, **477**, 5568
- Kakkad D., et al., 2018, *A&A*, **618**, A6
- Kashino D., Inoue A. K., 2019, *MNRAS*, **486**, 1053
- Kellermann K. I., Pauliny-Toth I. I. K., Williams P. J. S., 1969, *ApJ*, **157**, 1
- Kennicutt Jr. R. C., Bresolin F., Garnett D. R., 2003, *ApJ*, **591**, 801
- Kewley L. J., Dopita M. A., 2002, *ApJS*, **142**, 35
- Kewley L. J., Ellison S. L., 2008, *ApJ*, **681**, 1183
- Kewley L. J., Maier C., Yabe K., Ohta K., Akiyama M., Dopita M. A., Yuan T., 2013, *ApJ*, **774**, L10
- Kewley L. J., Nicholls D. C., Sutherland R. S., 2019, *ARA&A*, **57**, 511
- Kingdon J., Ferland G. J., Feibelman W. A., 1995, *ApJ*, **439**, 793
- Kobayashi M. I. N., Iwasaki K., Tomida K., Inoue T., Omukai K., Tokuda K., 2023, *ApJ*, **954**, 38
- Koski A. T., 1978, *ApJ*, **223**, 56
- Koutsoumpou E., Fernández-Ontiveros J. A., Dasyra K. M., Spinoglio L., 2025, *A&A*, **693**, A215
- Krabbe A. C., Pastoriza M. G., Winge C., Rodrigues I., Dors O. L., Ferreira D. L., 2011, *MNRAS*, **416**, 38
- Krabbe A. C., Oliveira C. B., Zinchenko I. A., Hernández-Jiménez J. A., Dors O. L., Hägele G. F., Cardaci M. V., Telles N. R., 2021, *MNRAS*, **505**, 2087
- Kraemer S. B., Wu C.-C., Crenshaw D. M., Harrington J. P., 1994, *ApJ*, **435**, 171
- Kroupa P., 2001, *MNRAS*, **322**, 231
- Kumari N., et al., 2024a, arXiv e-prints, p. arXiv:2406.11997
- Kumari N., Smit R., Leitherer C., Witstok J., Irwin M. J., Sirianni M., Aloisi A., 2024b, *MNRAS*, **529**, 781
- Kurk J. D., et al., 2007, *ApJ*, **669**, 32
- Kuźmicz A., Jamrozy M., 2021, *ApJS*, **253**, 25
- Labbe I., et al., 2024, arXiv e-prints, p. arXiv:2412.04557
- Lai S., et al., 2022, *MNRAS*, **513**, 1801
- Laor A., Netzer H., 1989, *MNRAS*, **238**, 897
- Lebouteiller V., et al., 2025, *A&A*, **695**, A31
- Lequeux J., Peimbert M., Rayo J. F., Serrano A., Torres-Peimbert S., 1979, *A&A*, **80**, 155
- Li Y., Leja J., Johnson B. D., Tacchella S., Davies R., Belli S., Park M., Emami R., 2024a, arXiv e-prints, p. arXiv:2405.04598
- Li S.-L., Grasha K., Krumholz M. R., Wisnioski E., Sutherland R. S., Kewley L. J., Chen Y.-M., Li Z., 2024b, *MNRAS*, **529**, 4993
- Li Y., Leja J., Johnson B. D., Tacchella S., Naidu R. P., 2024c, *ApJ*, **969**, L5
- Lisenfeld U., Völk H. J., 2000, *A&A*, **354**, 423
- Madau P., Dickinson M., 2014, *ARA&A*, **52**, 415
- Maiolino R., Mannucci F., 2019, *A&ARv*, **27**, 3
- Maiolino R., Juarez Y., Mujica R., Nagar N. M., Oliva E., 2003, *ApJ*, **596**, L155
- Maiolino R., et al., 2024, *A&A*, **691**, A145
- Malkan M. A., Sargent W. L. W., 1982, *ApJ*, **254**, 22
- Mathis J. S., 1986, *PASP*, **98**, 995
- Matsuoka K., Nagao T., Maiolino R., Marconi A., Taniguchi Y., 2009, *A&A*, **503**, 721
- Matsuoka K., Nagao T., Marconi A., Maiolino R., Mannucci F., Cresci G., Terao K., Ikeda H., 2018, *A&A*, **616**, L4
- McCarthy P. J., Spinrad H., van Breugel W., Liebert J., Dickinson M., Djorgovski S., Eisenhardt P., 1990, *ApJ*, **365**, 487
- McGaugh S. S., 1991, *ApJ*, **380**, 140
- Méndez-Delgado J. E., et al., 2024, *A&A*, **690**, A248
- Menezes R. B., Steiner J. E., Ricci T. V., da Silva P., 2022, *MNRAS*, **513**, 5935
- Mignoli M., et al., 2019, *A&A*, **626**, A9
- Mingozi M., et al., 2019, *A&A*, **622**, A146
- Monteiro A. F., Dors O. L., 2021, *MNRAS*, **508**, 3023
- Mouhcine M., Baldry I. K., Bamford S. P., 2007, *MNRAS*, **382**, 801
- Mountrichas G., Georgantopoulos I., 2024, *A&A*, **683**, A160
- Nagao T., Marconi A., Maiolino R., 2006a, *A&A*, **447**, 157
- Nagao T., Maiolino R., Marconi A., 2006b, *A&A*, **447**, 863
- Nagao T., Maiolino R., De Breuck C., Caselli P., Hatsukade B., Saigo K., 2012, *A&A*, **542**, L34
- Nakajima K., Maiolino R., 2022, *MNRAS*, **513**, 5134
- Nakane M., et al., 2025, arXiv e-prints, p. arXiv:2503.11457
- Napolitano L., et al., 2025, *A&A*, **693**, A50
- Nicholls D. C., Sutherland R. S., Dopita M. A., Kewley L. J., Groves B. A., 2017, *MNRAS*, **466**, 4403
- Niklas S., Klein U., Wielebinski R., 1997, *A&A*, **322**, 19

- Novak M., et al., 2017, [A&A](#), **602**, A5
- Oliveira S., Maciel W. J., 1986, [Ap&SS](#), **126**, 211
- Oliveira C. B., Dors O., Zinchenko I., Cardaci M., Hägele G., Morais I., Santos P., Almeida G., 2024, [Publ. Astron. Soc. Australia](#), **41**, e099
- Onodera M., et al., 2016, [ApJ](#), **822**, 42
- Onoue M., et al., 2020, [ApJ](#), **898**, 105
- Pagel B. E. J., Edmunds M. G., Blackwell D. E., Chun M. S., Smith G., 1979, [MNRAS](#), **189**, 95
- Papovich C., et al., 2022, [ApJ](#), **937**, 22
- Peimbert M., Costero R., 1969, Boletín de los Observatorios Tomantzinla y Tacubaya, **5**, 3
- Pérez-Díaz B., Pérez-Montero E., Fernández-Ontiveros J. A., Vílchez J. M., 2022, [A&A](#), **666**, A115
- Pérez-Díaz B., Pérez-Montero E., Fernández-Ontiveros J. A., Vílchez J. M., Amorín R., 2024, [Nature Astronomy](#), **8**, 368
- Pérez-Díaz B., Pérez-Montero E., Zinchenko I. A., Vílchez J. M., 2025, [A&A](#), **694**, A18
- Pérez-Montero E., Dors O. L., Vílchez J. M., García-Benito R., Cardaci M. V., Hägele G. F., 2019, [MNRAS](#), **489**, 2652
- Pérez-Montero E., Amorín R., Pérez-Díaz B., Vílchez J. M., García-Benito R., 2023, [MNRAS](#), **521**, 1556
- Pérez-Montero E., Fernández-Ontiveros J. A., Pérez-Díaz B., Vílchez J. M., Kumari N., Amorín R., 2024, [A&A](#), **684**, A40
- Pérez-Montero E., Fernández-Ontiveros J. A., Pérez-Díaz B., Vílchez J. M., Amorín R., 2025, [arXiv e-prints](#), p. arXiv:2503.09267
- Peterson B., 2006, The Broad-Line Region in Active Galactic Nuclei. Springer Berlin Heidelberg, Berlin, Heidelberg, pp 77–100, doi:10.1007/3-540-34621-X_3, https://doi.org/10.1007/3-540-34621-X_3
- Pilyugin L. S., 2000, [A&A](#), **362**, 325
- Pilyugin L. S., 2001, [A&A](#), **369**, 594
- Pilyugin L. S., Grebel E. K., 2016, [MNRAS](#), **457**, 3678
- Planck Collaboration et al., 2021, [A&A](#), **652**, C4
- Reddy N. A., Topping M. W., Sanders R. L., Shapley A. E., Brammer G., 2023, [ApJ](#), **952**, 167
- Revalski M., Crenshaw D. M., Kraemer S. B., Fischer T. C., Schmitt H. R., Machuca C., 2018, [ApJ](#), **856**, 46
- Richardson C. T., Allen J. T., Baldwin J. A., Hewett P. C., Ferland G. J., 2014, [MNRAS](#), **437**, 2376
- Rinaldi P., et al., 2025, [arXiv e-prints](#), p. arXiv:2504.01852
- Rizzuti F., Matteucci F., Molaro P., Cescutti G., Maiolino R., 2025, [A&A](#), **697**, A96
- Robertson P., Shields G. A., Blanc G. A., 2012, [ApJ](#), **748**, 48
- Rogers N. S. J., Skillman E. D., Pogge R. W., Berg D. A., Croxall K. V., Bartlett J., Arellano-Córdova K. Z., Moustakas J., 2022, [ApJ](#), **939**, 44
- Rogers N. S. J., Scarlata C. M., Skillman E. D., Eggen N. R., Jaskot A. E., Mehta V., Cannon J. M., 2023, [ApJ](#), **955**, 112
- Rupke D. S. N., Gültekin K., Veilleux S., 2017, [ApJ](#), **850**, 40
- Salpeter E. E., 1955, [ApJ](#), **121**, 161
- Sánchez S. F., et al., 2012, [A&A](#), **538**, A8
- Sánchez S. F., et al., 2015, [A&A](#), **574**, A47
- Sanders R. L., et al., 2016, [ApJ](#), **816**, 23
- Sanders R. L., et al., 2021, [ApJ](#), **914**, 19
- Sanders R. L., Shapley A. E., Topping M. W., Reddy N. A., Brammer G. B., 2023, [ApJ](#), **955**, 54
- Schindler J.-T., et al., 2020, [ApJ](#), **905**, 51
- Scholtz J., et al., 2023, [arXiv e-prints](#), p. arXiv:2311.18731
- Scholtz J., et al., 2025a, [MNRAS](#), **539**, 2463
- Scholtz J., et al., 2025b, [A&A](#), **697**, A175
- Senarath M. R., et al., 2021, [MNRAS](#), **503**, 2583
- Sharda P., Krumholz M. R., Wisnioski E., Acharya A., Federrath C., Forbes J. C., 2021, [MNRAS](#), **504**, 53
- Shields J. C., Kennicutt Jr. R. C., 1995, [ApJ](#), **454**, 807
- Shields J. C., Ferland G. J., Peterson B. M., 1995, [ApJ](#), **441**, 507
- Silcock M. S., et al., 2024, [arXiv e-prints](#), p. arXiv:2410.18193
- Silva M., Humphrey A., Lagos P., Morais S. G., 2020, [MNRAS](#), **495**, 4707
- Simon L. E., Hamann F., 2010, [MNRAS](#), **407**, 1826
- Skillman E. D., Berg D. A., Pogge R. W., Moustakas J., Rogers N. S. J., Croxall K. V., 2020, [ApJ](#), **894**, 138
- Storchi-Bergmann T., Calzetti D., Kinney A. L., 1994, [ApJ](#), **429**, 572
- Storchi-Bergmann T., Schmitt H. R., Calzetti D., Kinney A. L., 1998, [AJ](#), **115**, 909
- Sun F., et al., 2025, [ApJ](#), **980**, 12
- Tabatabaei F. S., et al., 2017, [ApJ](#), **836**, 185
- Tananbaum H., et al., 1979, [ApJ](#), **234**, L9
- Tang M., et al., 2025, [arXiv e-prints](#), p. arXiv:2505.06359
- Taylor C., Reynolds C. S., 2018, [ApJ](#), **855**, 120
- Terao K., Nagao T., Onishi K., Matsuoka K., Akiyama M., Matsuoka Y., Yamashita T., 2022, [ApJ](#), **929**, 51
- Thomas A. D., Dopita M. A., Kewley L. J., Groves B. A., Sutherland R. S., Hopkins A. M., Blanc G. A., 2018, [ApJ](#), **856**, 89
- Treiber H., et al., 2024, [arXiv e-prints](#), p. arXiv:2409.12232
- Tremonti C. A., et al., 2004, [ApJ](#), **613**, 898
- Troncoso P., et al., 2014, [A&A](#), **563**, A58
- Übler H., et al., 2024, [MNRAS](#), **531**, 355
- Vidal-García A., Plat A., Curtis-Lake E., Feltre A., Hirschmann M., Chevalard J., Charlton S., 2024, [MNRAS](#), **527**, 7217
- Villar Martín M., López Cobá C., Cazzoli S., Pérez Montero E., Cabrera Lavers A., 2024, [A&A](#), **690**, A397
- Wang W., Yuan Z., Yu H., Mao J., 2024, [A&A](#), **683**, A174
- Willott C. J., Rawlings S., Blundell K. M., Lacy M., 1999, [MNRAS](#), **309**, 1017
- Wu P.-F., Zahid H. J., Hwang H. S., Geller M. J., 2017, [MNRAS](#), **468**, 1881
- Wu Y., et al., 2023, [ApJ](#), **956**, L40
- Yang G., et al., 2017, [ApJ](#), **842**, 72
- York D. G., et al., 2000, [AJ](#), **120**, 1579
- Zajaček M., et al., 2019, [A&A](#), **630**, A83
- Zhang X., 2024, [ApJ](#), **960**, 108
- Zhu P., Kewley L. J., Sutherland R. S., 2023, [ApJ](#), **954**, 175
- Zhu P., Kewley L. J., Sutherland R. S., 2024, [ApJ](#), **977**, 187
- Zou F., Yu Z., Brandt W. N., Tak H., Yang G., Ni Q., 2024, [ApJ](#), **964**, 183
- de Gasperin F., Intema H. T., Frail D. A., 2018, [MNRAS](#), **474**, 5008
- do Nascimento J. C., et al., 2022, [MNRAS](#), **513**, 807
- van Zee L., Salzer J. J., Haynes M. P., O'Donoghue A. A., Balonek T. J., 1998, [AJ](#), **116**, 2805

This paper has been typeset from a \TeX / \LaTeX file prepared by the author.